JGR Solid Earth

RESEARCH ARTICLE
10.1029/2021JB023280

Propagating Seismic Waves in VTI Attenuating Media Using Fractional Viscoelastic Wave Equation

Ning Wang[1,2,3,4], Guangchi Xing[2], Tieyuan Zhu[2], Hui Zhou[3], and Ying Shi[1]

[1]School of earth sciences, Northeast Petroleum University, Daqing City, China, [2]Department of Geosciences, The Pennsylvania State University, University Park, PA, USA, [3]State Key Laboratory of Petroleum Resources and Prospecting, CNPC Key Lab of Geophysical Exploration, China University of Petroleum, Beijing, China, [4]Research Institute of Exploration and Development of Daqing Oilfield Company Ltd, Daqing, China

Key Points:

- We extend the existing viscoacoustic wave equation to viscoelastic wave equation with considering VTI velocity and attenuation
- Fractional operators with spatial-independent orders facilitate efficient viscoelastic modeling in heterogeneous media
- This proposed seismic wave modeling is demonstrated to be feasible at both 3D exploration and crust scales

Correspondence to:
T. Zhu and Y. Shi,
tyzhu@psu.edu;
shiying@nepu.edu.cn

Citation:
Wang, N., Xing, G., Zhu, T., Zhou, H., & Shi, Y. (2022). Propagating seismic waves in VTI attenuating media using fractional viscoelastic wave equation. *Journal of Geophysical Research: Solid Earth*, *127*, e2021JB023280. https://doi.org/10.1029/2021JB023280

Received 21 SEP 2021
Accepted 30 MAR 2022

Abstract Seismic velocity and attenuation anisotropy are ubiquitous in the crust and upper mantle, significantly modulating the characteristics of seismic wave propagation in the Earth's interior. Accurate seismic wave modeling of velocity and attenuation anisotropy is essential for the understanding of wave propagation in the Earth's interior as well as constructing global and region-scale seismic full waveform tomography. Here, we derive a decoupled fractional Laplacian (DFL) viscoelastic wave equation to characterize the Earth's frequency-independent Q behavior in the vertical transversely isotropic (VTI) media. We verify the accuracy of the proposed viscoelastic wave equation by 2D synthetic examples; to show its applicability in crustal-scale seismic modeling, we present an example of 3D seismic wave propagation in the realistic Salton Trough model. Through extensive numerical tests, we conclude that the proposed viscoelastic wave equation is superior in four aspects. First, the viscoelastic wave equation takes VTI anisotropy of both velocity and attenuation into account and can describe the strong direction-dependent attenuation. Second, our derivation contains spatially independent Laplacians, and thus the proposed wave equation enjoys higher simulation accuracy for heterogeneous Q media. Third, the new viscoelastic wave equation can decouple the amplitude decay and the phase distortion, which is appealing for improving the resolution in seismic imaging and inversion. Lastly, compared to viscoelastic wave equations with time-fractional operators, our scheme has higher computational efficiency by avoiding substantial wavefield storage.

Plain Language Summary The anisotropy of seismic velocity and attenuation is very common in the Earth's interior. Accurately characterizing seismic anisotropy during wave propagation is crucial for understanding the characteristics of seismic data and inversely mapping the Earth's interior. However, the state-of-art anisotropic viscoelastic wave equation suffers from either low accuracy or low computation efficiency. To address this issue, we derive a decoupled fractional Laplacian (DFL) viscoelastic wave equation to model the Earth's frequency-independent Q behavior in the vertical transversely isotropic (VTI) media. Several 2D synthetic examples indicate that our derivation enables to describe the strong direction-dependent attenuation and naturally adapt to complex heterogeneous media with high computation efficiency. We finally show its applicability in crustal-scale seismic modeling using a 3D realistic Salton Trough model.

1. Introduction

When seismic waves travel through the Earth's interior, from shallow crust to deep mantle to the core, both velocity and attenuation show direction-dependent characteristics (Anderson, 1989; Carcione, 1992; Stein & Wysession, 2003). The variation of seismic velocity and attenuation with directions is the intrinsic property of the Earth's interior structure for several reasons including the distribution of aligned fluid-filled fractures (Chichinina et al., 2009; Hosten et al., 1987), the preferential alignment of fractures (Liu et al., 1993; Lynn et al., 1999), and the anisotropic Zener relaxation of iron in the inner core (Mäkinen et al., 2014). Seismic anisotropy plays an important role in the identification of the inner core boundary (Yu & Wen, 2006), plate-motion deformation (Bao et al., 2020; Li et al., 2018), interpretation of rock physical properties (Piane et al., 2014), and fractured reservoirs (Guo & McMechan, 2017). To capture the anisotropy of velocity and attenuation simultaneously in seismic modeling and imaging, it is necessary to develop such an anisotropic viscoelastic wave equation.

In the past three decades, velocity anisotropy has been incorporated into seismic modeling and imaging practice (e.g., Carcione, 1995; Komatitsch et al., 2000; Thomsen, 1986; Tsvankin, 2012). It is straightforward to derive

a full anisotropic seismic wave equation by defining an elastic stiffness matrix or simplified acoustic-anisotropy wave equation by eliminating shear waves (Alkhalifah, 2000). However, attenuation anisotropy is often ignored in seismic modeling, even though this phenomenon has been extensively observed in laboratory rock measurements and field data (Carcione, 1992; Tao & King, 1990; Tsvankin, 2012; Zhubayev et al., 2016). Moreover, attenuation anisotropy is found to be more significant than the velocity anisotropy as a result of fractures (Chichinina et al., 2004; Lynn et al., 1999). The difficulty of formulating such an anisotropic viscoelastic wave equation is the involvement of a complex-valued stiffness matrix and its numerical solution.

The most common method to consider both velocity and attenuation anisotropy is predominantly developed based on mechanical (rheological) models, where frequency-independent Q behavior (McDonal et al., 1958; Spencer, 1981) of seismic wave propagation in the Earth's interior is approximated by a superposition of mechanical elements, such as Maxwell or standard linear solid (SLS) elements (Liu et al., 1976). Excellent pioneering work of time-domain viscoelastic modeling has been developed based on mechanical models (e.g., Blanch et al., 1995; Carcione et al., 1988; Day & Minster, 1984; Emmerich & Korn, 1987; Kristek et al., 2019; Kristek & Moczo, 2003), and detailed reviews of this development are provided by Carcione (2014) and Moczo et al. (2014). It is worth mentioning that the above rheological models (generalized Maxwell body and generalized Zener body) are essentially equivalent—shown by Moczo and Kristek (2005). Carcione (1990, 1992, 1995) established the wave equation theory of incorporating linear viscoelastic anisotropy and laid the foundation for later study of attenuation-velocity anisotropy media. Bai and Tsvankin (2016) developed a detailed numerical demonstration and analysis of vertical transversely isotropic (VTI) attenuation by 2D time-domain finite-difference modeling. Although mechanical models have been widely adopted in the literature of seismic forward modeling and inverse problems, it is worth pointing out two essential issues (Xing & Zhu, 2022): first, these mechanical model-based modeling approaches introduce the memory variables (most often $L = 3$ relaxation elements for seismology studies), which require significant computation time and memory, especially in 3D (e.g., Robertsson et al., 1994; Savage et al., 2010; Zhu et al., 2013); second, these approaches bring about difficulties in inverse problems as the Q is implicitly parameterized by a set of relaxation times (Fichtner and Van Driel, 2014).

Alternatively, a category of fractional wave equations built from the frequency-independent Q model (Caputo, 1967; Kjartansson, 1979) has drawn more attention because of its concise mathematical form and capacity of well describing the frequency-independent attenuation behavior. In earlier attempts, the fractional wave equation involving a time-fractional derivative has been studied in seismology, mathematics, and acoustic-bioengineering (e.g., Caputo, 1967; Caputo et al., 2011; Mainardi, 2010). The numerical implementation of the time-fractional derivative is hampered by the excessive memory requirement of storing the entire wave-field history. To avoid this storage, Chen and Holm (2004) resort to the fractional Laplacians to substitute the time-fractional operators with considering amplitude attenuation only. Treeby and Cox (2010) proposed to split the velocity dispersion and the amplitude attenuation effects by using the fractional Laplacians in a decoupled form.

In seismology, Zhu and his collaborators (Zhu & Carcione, 2014; Zhu & Harris, 2014) developed the decoupled fractional Laplacian (DFL) viscoelastic/viscoacoustic wave equations, which have benefited the attenuation-compensation seismic imaging (Li et al., 2016; Wang et al., 2017; Zhao et al., 2018; Zhu et al., 2014; Zhu & Sun, 2017) and inversion (Chen et al., 2020; Xing and Zhu, 2020, 2022; Xue et al., 2017; Yang et al., 2020). Subsequently, several decoupled-form viscous wave equations are proposed. For instance, Yang and Zhu (2018) derived a complex-valued wave equation by inserting the complex-valued velocity into acoustic wave equation and neglecting high-order terms related to Q; Li et al. (2019) developed a fractional viscoacoustic wave equation consisting of a single SLS; Mu et al. (2021) proposed a viscoelastic wave equation that describes the constant Q behavior via several variable-order fractional Laplacians. Taking Q anisotropy into account, Zhu (2017) first derived a time-fractional viscoelastic anisotropic wave equation. Further, Zhu and Bai (2019) and Qiao et al. (2019) replaced the time-fractional operators with efficient fractional spatial operators via different approximation methods. The latter derivation (Qiao et al., 2019) is built on the assumption that the anisotropy characteristics of attenuation and velocity are similar and the Thomsen parameter of δ is small. In all above mentioned derived fractional wave equations, the power terms of DFL are mixed-domain (spatial and wavenumber) operators, which is challenging to be numerically solved in an efficient manner. To improve the efficiency, several intermediate approaches (e.g., Chen et al., 2016; Sun et al., 2015; Wang et al., 2018; Wang et al., 2020; Zhang et al., 2020) have been proposed. Recently, Xing and Zhu (2019) developed a novel spatial-independent-order DFL viscoacoustic wave equation that fully avoids the difficulty of computing mixed-domain operators.

In this paper, to propagate P-, S-, converted waves, and surface waves, we derive a VTI viscoelastic wave equation to incorporate both velocity and attenuation anisotropy. The proposed DFL viscoelastic wave equation not only inherits the advantages of decoupled wave amplitude and phase dispersion, but also has the ability to characterize strong VTI attenuation. We also analyze the stability condition using the eigenvalue method (Gazdag, 1981) and describe the numerical implementation of the staggered-grid pseudo-spectral (SGPS) method for solving the proposed wave equations. The propagation of surface waves with free boundary is based on the vacuum formalism (Zahradník et al., 1993). We use a series of 2D models with different levels of model complexities to demonstrate the accuracy of the proposed wave equations, and a 3D Salton Trough model to show the feasibility in crustal-scale seismic modeling. By comparing the computational cost of 2D and 3D synthetic tests, we show that the proposed VTI-DFL wave equations can achieve a few 10 times faster than the time-fractional based wave equations with MATLAB codes and even five hundred times faster with a GPU CUDA code.

The rest of this paper is organized as follows. In the methodology section, we provide a detailed description of the proposed VTI-DFL viscoelastic wave equation followed by analyzing the stability conditions, detailing its numerical implementation, and summarizing its advantages. In the numerical examples, we conduct a series of experiments to verify the accuracy and demonstrate the advantages of the proposed viscoelastic wave equations. Then, we discuss computational efficiency. Finally, we draw conclusions.

2. Theory

2.1. Dispersion Relation of the Frequency-Independent Q Model

Both laboratory experiments and *in-situ* seismic surveys (e.g., McDonal et al., 1958) suggested that seismic Q is almost independent of frequency over the narrow seismic frequency band. According to the Kjartansson's frequency-independent Q model (Kjartansson, 1979), the dispersion relation between the complex wavenumber k and the angular frequency ω is

$$k(\omega) = \frac{1}{c}\omega_0^{\gamma}\omega^{1-\gamma}e^{-i\pi\gamma/2}, \tag{1}$$

where attenuation strength $\gamma = \arctan Q^{-1}/\pi$; the "propagation velocity" c is related to the phase velocity c_0 at frequency ω_0 by $c = c_0\cos(\pi\gamma/2)$. To achieve computational efficiency and accuracy, Xing and Zhu (2019) proposed a viscoacoustic wave equation, which can be expressed in frequency-wavenumber domain as

$$\omega^2 = d_1 k + d_2 k^2 + d_3 k^3 + d_4(i\omega)k + d_5(i\omega)k^2, \tag{2}$$

where $(d_1, d_2, d_3, d_4, d_5)$ are real parameters related to media properties (i.e., reference frequency ω_0, velocity c and attenuation strength γ). To make Equation 2 to satisfy Equation 1, Xing and Zhu (2019) searched for optimized parameters $(d_1, d_2, d_3, d_4, d_5)$ so that the solution of Equation 2 approximates the Kjartansson wavenumber k in Equation 1 for all the frequencies in the seismic range. These coefficients are derived as follows:

$$(d_1, d_2, d_3, d_4, d_5) = \left(-\gamma c\omega_0, c^2, \gamma c^3\omega_0^{-1}, \pi\gamma c, \pi\gamma^2 c^2\omega_0^{-1}\right). \tag{3}$$

Thus, the approximate dispersion relation (Equation 2) can well capture the wavefield behavior described by the Kjartansson model (Equation 1) in terms of dynamic dissipation (imaginary part of k) and kinematic dispersion (real part of k). The detailed derivation of Equation 3 can be found in Xing and Zhu (2019). We have to emphasize that the wavenumber k has a constant power (i.e., spatially independent) in Equation 2, which leads to fractional Laplacian operators with spatially independent-order in the time-space domain (Section 2.2) and thus guarantees the accuracy when handling heterogeneous Q media.

2.2. Isotropic Viscoelastic Wave Equation

We generalize the viscoacoustic dispersion relation (Equation 2) to describe both P- and S-modes of the viscoelastic wave:

$$\omega^2 = d_{\theta,1}k + d_{\theta,2}k^2 + d_{\theta,3}k^3 + d_{\theta,4}(i\omega)k + d_{\theta,5}(i\omega)k^2, \tag{4}$$

where $\theta = P$ or s represents P- or S-wave, respectively. Thus, the corresponding parameters are given by

$$(d_{\theta,1}, d_{\theta,2}, d_{\theta,3}, d_{\theta,4}, d_{\theta,5}) = \left(-\gamma_\theta c_\theta \omega_0, c_\theta^2, \gamma_\theta c_\theta^3 \omega_0{}^{-1}, \pi\gamma_\theta c_\theta, \pi\gamma_\theta^2 c_\theta^2 \omega_0{}^{-1}\right). \tag{5}$$

where c_θ and γ_θ are associated propagation velocity and attenuation strength, respectively. For each wave mode, the complex modulus M_θ relates to the complex wavenumber k as

$$M_\theta = \rho\frac{\omega^2}{k^2} = C_\theta\frac{\omega^2}{c_\theta^2 k^2}, \tag{6}$$

where $C_\theta = \rho c_\theta^2$ is a real parameter with modulus/stiffness dimension. Substituting the dispersion relation (Equation 4) into Equation 6 leads to the complex modulus

$$M_\theta = C_\theta\frac{1}{c_\theta^2}\left(d_{\theta,1}k^{-1} + d_{\theta,2} + d_{\theta,3}k + d_{\theta,4}(i\omega)k^{-1} + d_{\theta,5}(i\omega)\right). \tag{7}$$

This expression of complex modulus M_θ in the frequency-wavenumber domain can be transformed into a constitutive operator L_θ in the time-space domain

$$L_\theta = C_\theta\frac{1}{c_\theta^2}\left(d_{\theta,1}\left(-\nabla^2\right)^{-\frac{1}{2}} + d_{\theta,2} + d_{\theta,3}\left(-\nabla^2\right)^{\frac{1}{2}} + d_{\theta,4}\left(-\nabla^2\right)^{-\frac{1}{2}}\frac{\partial}{\partial t} + d_{\theta,5}\frac{\partial}{\partial t}\right). \tag{8}$$

The constitutive relation of both wave modes can thus be written with the constitutive operators (Wang et al., 2016):

$$\begin{cases}\sigma_{ij}^p = L_p\delta_{ij}e_{kk}\\ \sigma_{ij}^s = L_s\left(2e_{ij} - 2\delta_{ij}e_{kk}\right)\end{cases}, \tag{9}$$

where σ_{ij}^p and σ_{ij}^s denote the stress tensors for P- and S-modes, respectively, e_{kk} and e_{ij} are strain tensors, and δ_{ij} is the Kronecker delta. The indices i, j, k denote to spatial coordinates. The P-S coupled stress tensor is obtained by summing σ_{ij}^p and σ_{ij}^s, written as:

$$\sigma_{ij} = \sigma_{ij}^p + \sigma_{ij}^s = L_p\delta_{ij}e_{kk} + L_s\left(2e_{ij} - 2\delta_{ij}e_{kk}\right). \tag{10}$$

In the meantime, we have the conservation of momentum

$$\frac{\partial^2 u_i}{\partial t^2} = \frac{1}{\rho}\frac{\partial\sigma_{ij}}{\partial x_j}, \tag{11}$$

and the definition of the strain tensor

$$e_{ij} = \frac{1}{2}\left(\frac{\partial u_i}{\partial x_j} + \frac{\partial u_j}{\partial x_i}\right), \tag{12}$$

where u_i denotes the particle displacement of the ith direction. Combining Equations 10–12, we obtain the spatially-independent-order DFL viscoelastic wave equation

$$\begin{cases}\dfrac{\partial v_i}{\partial t} = \dfrac{1}{\rho}\dfrac{\partial\sigma_{ij}}{\partial x_j},\\ \dot{e}_{ij} = \dfrac{1}{2}\left(\dfrac{\partial v_i}{\partial x_j} + \dfrac{\partial v_j}{\partial x_i}\right)\\ \dfrac{\partial\sigma_{ij}}{\partial t} = L_p\delta_{ij}\dot{e}_{kk} + L_s\left(2\dot{e}_{ij} - 2\delta_{ij}\dot{e}_{kk}\right)\end{cases}, \tag{13}$$

where the strain rate $\dot{e}_{ij} = \frac{\partial e_{ij}}{\partial t}$ and the particle velocity $v_i = \frac{\partial u_i}{\partial t}$. By eliminating $\dot{e}_{ij}$, it is convenient to write the 2D DFL viscoelastic wave equation in the following first-order system:

$$\begin{cases} \rho\dfrac{\partial v_x}{\partial t} = \dfrac{\partial \sigma_{xx}}{\partial x} + \dfrac{\partial \sigma_{xz}}{\partial z} \\ \rho\dfrac{\partial v_z}{\partial t} = \dfrac{\partial \sigma_{xz}}{\partial x} + \dfrac{\partial \sigma_{zz}}{\partial z} \\ \dfrac{\partial \sigma_{xx}}{\partial t} = L_p\left(\dfrac{\partial v_x}{\partial x} + \dfrac{\partial v_z}{\partial z}\right) - 2L_s\dfrac{\partial v_z}{\partial z} \\ \dfrac{\partial \sigma_{zz}}{\partial t} = L_p\left(\dfrac{\partial v_x}{\partial x} + \dfrac{\partial v_z}{\partial z}\right) - 2L_s\dfrac{\partial v_x}{\partial x} \\ \dfrac{\partial \sigma_{xz}}{\partial t} = L_s\left(\dfrac{\partial v_z}{\partial x} + \dfrac{\partial v_x}{\partial z}\right) \end{cases}. \tag{14}$$

Note that the original DFL viscoelastic wave equation (Zhu & Carcione, 2014) contains spatially-dependent-order fractional Laplacians (the power terms of the Laplacian operators are functions of γ), which introduces spatial-wavenumber mixed-domain problems, concerned in many following studies (Chen et al., 2016; Sun et al., 2015; Xing & Zhu, 2019; Yang & Zhu, 2018; Yao et al., 2016). Zhu and Harris (2014) adopt the average value of γ to approximate the fractional power terms γ (here, we refer it average scheme for short). The average scheme works well for homogeneous or smooth Q models, but it introduces significant simulation errors for sharp Q-contrast models (Chen et al., 2016). This problem is naturally avoided in our proposed spatially-independent-order DFL viscoelastic wave equation (Equation 14), where the power terms of fractional Laplacians are constant (Equation 8).

2.3. VTI Viscoelastic Wave Equation

Here, we consider a particular type of anisotropy with a vertical transversely isotropic (VTI) symmetry that is common in the upper crust (Tsvankin, 2012) and deep mantle (Romanowicz & Wenk, 2017). A medium with such symmetry could be a laminated fabric defined by aligned minerals, such as sheet silicates, and/or lithological layering.

2.3.1. Elastic VTI Stiffness Matrix

The structure of stiffness tensor determines the velocity and polarization of seismic waves for any propagation direction (Tsvankin, 2012). The most general anisotropic model is triclinic, whose stiffness matrix consists of 21 independent elements. The stiffness matrix of triclinic media has the following abbreviated Voigt notation form

$$\mathbf{C} = \begin{bmatrix} C_{11} & C_{12} & C_{13} & C_{14} & C_{15} & C_{16} \\ C_{12} & C_{22} & C_{23} & C_{24} & C_{25} & C_{26} \\ C_{13} & C_{23} & C_{33} & C_{34} & C_{35} & C_{36} \\ C_{14} & C_{24} & C_{34} & C_{44} & C_{45} & C_{46} \\ C_{15} & C_{25} & C_{35} & C_{45} & C_{55} & C_{56} \\ C_{16} & C_{26} & C_{36} & C_{46} & C_{56} & C_{66} \end{bmatrix}, \tag{15}$$

According to the number of symmetry axes, the stiffness matrix of 3D VTI media in abbreviated Voigt notation form is

$$\mathbf{C}=\begin{bmatrix} C_{11} & C_{11}\text{-}2C_{66} & C_{13} & 0 & 0 & 0 \\ C_{11}\text{-}2C_{66} & C_{11} & C_{13} & 0 & 0 & 0 \\ C_{13} & C_{13} & C_{33} & 0 & 0 & 0 \\ 0 & 0 & 0 & C_{55} & 0 & 0 \\ 0 & 0 & 0 & 0 & C_{55} & 0 \\ 0 & 0 & 0 & 0 & 0 & C_{66} \end{bmatrix}. \tag{16}$$

With the assumption of weak anisotropy (Thomsen, 1986), the relation between the velocity and the elastic stiffness can be simplified as

$$\begin{gathered} C_{11}=\rho c_{p\mathrm{II}}^2, C_{33}=\rho c_{p\perp}^2, C_{55}=\rho c_s^2, C_{66}=(1+2\gamma)C_{55}, \\ C_{13}=\sqrt{2\delta C_{33}\left(C_{33}-C_{55}\right)+\left(C_{33}-C_{55}\right)^2}-C_{55}, \end{gathered} \tag{17}$$

where $c_{p\perp}$ and $c_{p\mathrm{II}}$ represent the P-wave velocity at the vertical and horizontal directions, and $c_{p\perp}=\frac{c_{p\mathrm{II}}}{\sqrt{1+2\epsilon}}$; c_s denotes the SV-wave velocity. ϵ , γ and δ are the Thomsen parameters under the assumption of weak anisotropy (Thomsen, 1986). Note that the Thomsen parameters are usually less than 0.2. If only considering elastic waves in the x-z plane, Equation 16 reduces to

$$\mathbf{C}=\begin{bmatrix} C_{11} & C_{13} & 0 \\ C_{13} & C_{33} & 0 \\ 0 & 0 & C_{55} \end{bmatrix}. \tag{18}$$

2.3.2. VTI Anisotropic Attenuation

Similarly, the Q matrix is proposed by Zhu and Tsvankin (2006) to describe the direction-dependent attenuation. In a 3D VTI medium, the Q matrix can be expressed as

$$\mathbf{Q}=\begin{bmatrix} Q_{11} & Q_{12} & Q_{13} & 0 & 0 & 0 \\ Q_{12} & Q_{11} & Q_{13} & 0 & 0 & 0 \\ Q_{13} & Q_{13} & Q_{33} & 0 & 0 & 0 \\ 0 & 0 & 0 & Q_{55} & 0 & 0 \\ 0 & 0 & 0 & 0 & Q_{55} & 0 \\ 0 & 0 & 0 & 0 & 0 & Q_{66} \end{bmatrix}, \tag{19}$$

where Q_{11} and Q_{33} denote P-wave quality factors at the horizontal and vertical directions, respectively; Q_{55} and Q_{66} represent the SV-wave and the SH-wave quality factors. Under the assumption of weak attenuation anisotropy (i.e., Q_{13} is of the same magnitude as Q_{33} and Q_{55}), Zhu and Tsvankin (2006) derived the relations between Q_{11}, Q_{33}, Q_{12}, and Q_{13} using the Thomsen style attenuation anisotropy parameters of ϵ_Q, γ_Q and δ_Q, given as

$$Q_{11}=\frac{Q_{33}}{1+\epsilon_Q}, \tag{20}$$

$$Q_{66}=\frac{Q_{55}}{1+\gamma_Q}, \tag{21}$$

$$Q_{12}=Q_{11}\frac{C_{11}-2C_{66}}{C_{11}-2C_{66}\frac{Q_{11}}{Q_{66}}}, \tag{22}$$

$$Q_{13} = \frac{2Q_{33}}{\left(\delta_Q C_{33}\left(C_{33}-C_{55}\right) - \frac{Q_{33}-Q_{55}}{Q_{55}}\frac{C_{55}\left(C_{13}+C_{33}\right)^2}{C_{33}-C_{55}}\right)\frac{1}{C_{13}\left(C_{13}+C_{55}\right)}+2}. \tag{23}$$

If only considering attenuation in the x-z plane, the Q matrix of 2D VTI media is

$$\mathbf{Q} = \begin{bmatrix} Q_{11} & Q_{13} & 0 \\ Q_{13} & Q_{33} & 0 \\ 0 & 0 & Q_{55} \end{bmatrix}. \tag{24}$$

2.3.3. VTI-DFL Viscoelastic Wave Equation

Different from the anisotropic elastic media (elements of stiffness matrix $\mathbf{C}$ are real values), the anisotropic viscoelastic media introduce complex-valued stiffness matrix (or complex moduli, denoted by $\tilde{\mathbf{C}}$). Each element of $\tilde{\mathbf{C}}$ can be generalized from the $\mathbf{C}$ (Carcione, 1990) as following:

$$\tilde{C}_{ij} = C_{ij}\cos^2\left(\pi\gamma_{ij}/2\right)\left(\frac{i\omega}{\omega_0}\right)^{2\gamma_{ij}}, \tag{25}$$

where

$$\gamma_{ij} = \frac{1}{\pi}\arctan\frac{1}{Q_{ij}}. \tag{26}$$

The above complex-valued stiffness matrix in Equation 25 can be parameterized to describe general Q anisotropy in the anisotropic time-fractional (VTI-TF) viscoelastic wave equation (Zhu, 2017). However, as we stated, this type of time-fractional wave equation demands huge computational memory. Below we show the derivation of the VTI viscoelastic wave equation with decoupled fractional Laplacian operators (VTI-DFL).

The constitutive relation of a 2D VTI medium in the frequency-wavenumber domain is:

$$\tilde{\sigma}_{xx} = \tilde{C}_{11}\left(\tilde{e}_{xx}+\tilde{e}_{zz}\right) + \frac{1}{2}\left(\tilde{C}_{11}-\tilde{C}_{13}\right)\left(-2\tilde{e}_{zz}\right), \tag{27}$$

$$\tilde{\sigma}_{zz} = \tilde{C}_{33}\left(\tilde{e}_{xx}+\tilde{e}_{zz}\right) + \frac{1}{2}\left(\tilde{C}_{33}-\tilde{C}_{13}\right)\left(-2\tilde{e}_{xx}\right), \tag{28}$$

$$\tilde{\sigma}_{xz} = \tilde{C}_{55}\tilde{e}_{xz}, \tag{29}$$

Decomposing Equation 27 into P- and S-components, we have

$$\tilde{\sigma}_{p,xx} = \tilde{C}_{11}\left(\tilde{e}_{xx}+\tilde{e}_{zz}\right), \tag{30}$$

$$\tilde{\sigma}_{s,xx} = \left(\tilde{C}_{13}-\tilde{C}_{11}\right)\tilde{e}_{zz}. \tag{31}$$

Equation 30 is associated with velocity $c_{p\mathrm{II}}$, from Equation 7. We define $\tilde{C}_{11}$ as

$$\tilde{C}_{11} = C_{11}\frac{1}{c_{p\mathrm{II}}^2}\left(-\gamma_{11}c_{p\mathrm{II}}\omega_0 k^{-1} + c_{p\mathrm{II}}^2 + \gamma_{11}c_{p\mathrm{II}}^3\omega_0^{-1}k + \pi\gamma_{11}c_{p\mathrm{II}}(i\omega)k^{-1} + \pi\gamma_{11}^2c_{p\mathrm{II}}^2\omega_0^{-1}(i\omega)\right). \tag{32}$$

Equation 31 is associated with velocity c_s, and $\tilde{C}_{11}$ and $\tilde{C}_{13}$ are expressed as

$$\tilde{C}_{11} = C_{11}\frac{1}{c_s^2}\left(-\gamma_{11}c_s\omega_0 k^{-1} + c_s^2 + \gamma_{11}c_s^3\omega_0^{-1}k + \pi\gamma_{11}c_s(i\omega)k^{-1} + \pi\gamma_{11}^2c_s^2\omega_0^{-1}(i\omega)\right), \tag{33}$$

$$\tilde{C}_{13} = C_{13}\frac{1}{c_s^2}\left(-\gamma_{13}c_s\omega_0 k^{-1} + c_s^2 + \gamma_{13}c_s^3\omega_0^{-1}k + \pi\gamma_{13}c_s(i\omega)k^{-1} + \pi\gamma_{13}^2c_s^2\omega_0^{-1}(i\omega)\right). \tag{34}$$

With these, we then transform Equation 27 into the time-space domain

$$\sigma_{xx} = M_{11}\left(e_{xx} + e_{zz}\right) + \left(M_{13} - \overline{M}_{11}\right) e_{zz}. \tag{35}$$

We repeat similar manipulations for Equations 28 and 29. Combining with Equations 11 and 12 yields the following 2D spatially-independent-order VTI-DFL viscoelastic wave equation in the first-order formulation

$$\begin{cases} \rho\dfrac{\partial v_x}{\partial t} = \dfrac{\partial \sigma_{xx}}{\partial x} + \dfrac{\partial \sigma_{xz}}{\partial z} \\ \rho\dfrac{\partial v_z}{\partial t} = \dfrac{\partial \sigma_{xz}}{\partial x} + \dfrac{\partial \sigma_{zz}}{\partial z} \\ \dfrac{\partial \sigma_{xx}}{\partial t} = M_{11}\left(\dfrac{\partial v_x}{\partial x} + \dfrac{\partial v_z}{\partial z}\right) + \left(M_{13} - \overline{M}_{11}\right)\dfrac{\partial v_z}{\partial z} \\ \dfrac{\partial \sigma_{zz}}{\partial t} = M_{33}\left(\dfrac{\partial v_x}{\partial x} + \dfrac{\partial v_z}{\partial z}\right) + \left(M_{13} - \overline{M}_{33}\right)\dfrac{\partial v_x}{\partial x} \\ \dfrac{\partial \sigma_{xz}}{\partial t} = M_{55}\left(\dfrac{\partial v_z}{\partial x} + \dfrac{\partial v_x}{\partial z}\right) \end{cases}, \tag{36}$$

with

$$\begin{cases} M_{11} = C_{11}\left(-\dfrac{\gamma_{11}\omega_0}{c_{p\parallel}}\left(-\nabla^2\right)^{-\frac{1}{2}} + 1 + \gamma_{11}\dfrac{c_{p\parallel}}{\omega_0}\left(-\nabla^2\right)^{\frac{1}{2}} + \dfrac{\pi\gamma_{11}}{c_{p\parallel}}\left(-\nabla^2\right)^{-\frac{1}{2}}\dfrac{\partial}{\partial t} + \dfrac{\pi\gamma_{11}^2}{\omega_0}\dfrac{\partial}{\partial t}\right) \\ M_{33} = C_{33}\left(-\dfrac{\gamma_{33}\omega_0}{c_{p\perp}}\left(-\nabla^2\right)^{-\frac{1}{2}} + 1 + \gamma_{33}\dfrac{c_{p\perp}}{\omega_0}\left(-\nabla^2\right)^{\frac{1}{2}} + \dfrac{\pi\gamma_{33}}{c_{p\perp}}\left(-\nabla^2\right)^{-\frac{1}{2}}\dfrac{\partial}{\partial t} + \dfrac{\pi\gamma_{33}^2}{\omega_0}\dfrac{\partial}{\partial t}\right) \\ M_{55} = C_{55}\left(-\dfrac{\gamma_{55}\omega_0}{c_s}\left(-\nabla^2\right)^{-\frac{1}{2}} + 1 + \gamma_{55}\dfrac{c_s}{\omega_0}\left(-\nabla^2\right)^{\frac{1}{2}} + \dfrac{\pi\gamma_{55}}{c_s}\left(-\nabla^2\right)^{-\frac{1}{2}}\dfrac{\partial}{\partial t} + \dfrac{\pi\gamma_{55}^2}{\omega_0}\dfrac{\partial}{\partial t}\right) \\ M_{13} = C_{13}\left(-\dfrac{\gamma_{13}\omega_0}{c_s}\left(-\nabla^2\right)^{-\frac{1}{2}} + 1 + \gamma_{13}\dfrac{c_s}{\omega_0}\left(-\nabla^2\right)^{\frac{1}{2}} + \dfrac{\pi\gamma_{13}}{c_s}\left(-\nabla^2\right)^{-\frac{1}{2}}\dfrac{\partial}{\partial t} + \dfrac{\pi\gamma_{13}^2}{\omega_0}\dfrac{\partial}{\partial t}\right) \\ \bar{M}_{11} = C_{11}\left(-\dfrac{\gamma_{11}\omega_0}{c_s}\left(-\nabla^2\right)^{-\frac{1}{2}} + 1 + \gamma_{11}\dfrac{c_s}{\omega_0}\left(-\nabla^2\right)^{\frac{1}{2}} + \dfrac{\pi\gamma_{11}}{c_s}\left(-\nabla^2\right)^{-\frac{1}{2}}\dfrac{\partial}{\partial t} + \dfrac{\pi\gamma_{11}^2}{\omega_0}\dfrac{\partial}{\partial t}\right) \\ \bar{M}_{33} = C_{33}\left(-\dfrac{\gamma_{33}\omega_0}{c_s}\left(-\nabla^2\right)^{-\frac{1}{2}} + 1 + \gamma_{33}\dfrac{c_s}{\omega_0}\left(-\nabla^2\right)^{\frac{1}{2}} + \dfrac{\pi\gamma_{33}}{c_s}\left(-\nabla^2\right)^{-\frac{1}{2}}\dfrac{\partial}{\partial t} + \dfrac{\pi\gamma_{33}^2}{\omega_0}\dfrac{\partial}{\partial t}\right) \end{cases}, \tag{37}$$

Note that when $Q_{ij} \to \infty$ ($\gamma_{ij} \to 0$), Equation 37 reduces to

$$\begin{cases} M_{11} = \overline{M}_{11} = C_{11} \\ M_{33} = \overline{M}_{33} = C_{33} \\ M_{55} = C_{55} \\ M_{13} = C_{13} \end{cases}. \tag{38}$$

and Equation 36 reduces to the classic VTI elastic wave equation. When we further set the Thomsen parameters to zero, Equation 36 further reduces to the isotropic elastic wave equation. We also provide full three-dimension formulation of DFL and VTI-DFL viscoelastic equations in Appendix A.

2.4. Stability Condition

We analyze the stability of the proposed DFL and VTI-DFL viscoelastic wave equations using the eigenvalue method (Gazdag, 1981). Equations 14 and 36 can be rewritten into the following second-order form

$$\frac{\partial^2 \mathbf{\Phi}}{\partial t^2} = \mathbf{B}\mathbf{\Phi}, \tag{39}$$

where $\mathbf{\Phi} = [v_x, v_z, \sigma_{xx}, \sigma_{zz}, \sigma_{xz}]^{\mathrm{T}}$, and $\mathbf{B}$ is the attenuation operator matrix. We discretize the second-order time derivative in Equation 39 by the FD operator, and perform Fourier transform to the spatial derivatives. Then we have

$$\left[\frac{4}{\Delta t^2}\sin^2\left(\frac{\omega\Delta t}{2}\right)\mathbf{E} - \tilde{\mathbf{B}}\right]\mathbf{\Phi} = 0, \tag{40}$$

where $\mathbf{E}$ is a unit matrix, and the expression of $\tilde{\mathbf{B}}$ is shown as Equation D1 and D4 in Appendix D. Equation 39 is a hyperbolic equation, a non-singular matrix $\mathbf{S}$ must exist and makes $\tilde{\mathbf{B}} = \mathbf{S}^{-1}\mathbf{\Lambda}\mathbf{S}$, where $\mathbf{\Lambda}$ is a diagonal matrix consisting of eigenvalues λ_i of matrix $\tilde{\mathbf{B}}$. Thus, we have

$$\mathbf{S}^{-1}\left[\frac{4}{\Delta t^2}\sin^2\left(\frac{\omega\Delta t}{2}\right)\mathbf{E} - \mathbf{\Lambda}\right]\mathbf{S}\mathbf{\Phi} = 0, \tag{41}$$

Obtaining non-zero solutions requires $\det\left(\mathbf{S}^{-1}\left[\frac{4}{\Delta t^2}\sin^2\left(\frac{\omega\Delta t}{2}\right)\mathbf{E} - \mathbf{\Lambda}\right]\mathbf{S}\right) = 0$ (i.e. $\det\left(\frac{4}{\Delta t^2}\sin^2\left(\frac{\omega\Delta t}{2}\right)\mathbf{E} - \mathbf{\Lambda}\right) = 0$), yielding to

$$\left|\frac{4}{\Delta t^2}\sin^2\left(\frac{\omega\Delta t}{2}\right)\mathbf{E} - \lambda_i\right| = 0. \tag{42}$$

Since $0 \le \sin^2\left(\frac{\omega\Delta t}{2}\right) \le 1$,

$$0 \le \frac{4}{\Delta t^2}\lambda_i \le 1. \tag{43}$$

The expression of λ_i is shown as Equation D3 and D6 in Appendix D. Setting density $\rho = 1g/cm^3$ for simplicity, and selecting the wavenumber as the Nyquist spatial wavenumber of $k = \pi/\Delta x$, we obtain the stability condition of the VTI-DFL viscoelastic wave equation as follows

$$\Delta t \le \frac{\sqrt{2}\Delta x}{\pi\sqrt{G}}, \tag{44}$$

with $G = \frac{1}{4}\left\{G_1 + G_3 + 2G_5 + \sqrt{(G_1 - G_3)^2 + 4(G_2 + G_5)(G_4 + G_5)}\right\}$, and parameters of G1 to G5 are defined in Appendix D. The stability condition of the DFL viscoelastic wave equation is

$$\Delta t \le \frac{\sqrt{2}\Delta x}{\pi\sqrt{D}}, \tag{45}$$

where $D = d_{p,1}k^{-1} + d_{p,2} + d_{p,3}k + \left(d_{p,4}k^{-1} + d_{p,5}\right)ikv$, $v = \max\{c_p, c_s\}$, and parameters of $d_{p,1}$ to $d_{p,5}$ can be found in Equation 5. Particularly, as $\gamma = 0$, and the anisotropic parameters $(\epsilon, \delta, \varepsilon_Q, \delta_Q)$ equal to zero, G and D reduce to $c^2_{\max}$, and Equations 44 and 45 reduce to the stability condition of the classical elastic wave equation (Gazdag, 1981):

$$\Delta t \le \frac{\sqrt{2}\Delta x}{\pi c_{\max}}. \tag{46}$$

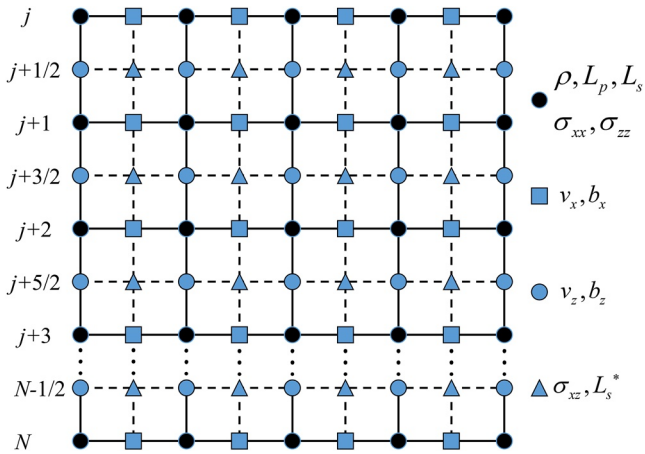

Figure 1. Layout of the wavefield variables and medium parameters on staggered grids in 2D Cartesian coordinates.

2.5. Numerical Implementation

We use the SGPS method to solve the proposed viscoelastic wave equation. Taking Equation 14 as an example, we rewrite Equation 14 as

$$\begin{cases} \dfrac{\partial v_x}{\partial t} = b_x\left(\dfrac{\partial \sigma_{xx}}{\partial x} + \dfrac{\partial \sigma_{xz}}{\partial z}\right) \\ \dfrac{\partial v_z}{\partial t} = b_z\left(\dfrac{\partial \sigma_{xz}}{\partial x} + \dfrac{\partial \sigma_{zz}}{\partial z}\right) \\ \dfrac{\partial \sigma_{xx}}{\partial t} = L_p\left(\dfrac{\partial v_x}{\partial x} + \dfrac{\partial v_z}{\partial z}\right) - 2L_s\dfrac{\partial v_z}{\partial z} \\ \dfrac{\partial \sigma_{zz}}{\partial t} = L_p\left(\dfrac{\partial v_x}{\partial x} + \dfrac{\partial v_z}{\partial z}\right) - 2L_s\dfrac{\partial v_x}{\partial x} \\ \dfrac{\partial \sigma_{xz}}{\partial t} = L_s^*\left(\dfrac{\partial v_z}{\partial x} + \dfrac{\partial v_x}{\partial z}\right) \end{cases}. \tag{47}$$

Figure 1 shows the distribution of all variables defined in Equation 47. We use the harmonic-averaging scheme (Moczo et al., 2002) to compute heterogeneous model parameters. Thus, we have

$$\begin{aligned} b_{xi+\frac{1}{2},j} &= \begin{cases} \dfrac{2}{\rho_{i+1,j} + \rho_{i,j}} & if\ (\rho_{i+1,j} \neq 0 \text{ or } \rho_{i,j} \neq 0) \\ 0 & if\ (\rho_{i+1,j} = 0, \rho_{i,j} = 0) \end{cases}, \\ b_{zi,j+\frac{1}{2}} &= \begin{cases} \dfrac{2}{\rho_{i,j} + \rho_{i,j+1}} & if\ (\rho_{i,j+1} \neq 0 \text{ or } \rho_{i,j} \neq 0) \\ 0 & if\ (\rho_{i,j+1} = 0, \rho_{i,j} = 0) \end{cases}, \end{aligned} \tag{48}$$

$$L_{s^*_{i+\frac{1}{2},j+\frac{1}{2}}} = \begin{cases} \left[\dfrac{1}{4}\left(\dfrac{1}{L_{s_{i,j}}} + \dfrac{1}{L_{s_{i+1,j}}} + \dfrac{1}{L_{s_{i,j+1}}} + \dfrac{1}{L_{s_{i+1,j+1}}}\right)\right]^{-1}, \text{if} L_{s_{i,j}} L_{s_{i+1,j}} L_{s_{i,j}} + 1 L_{s_{i+1,j+1}} \neq 0 \\ 0 \qquad\qquad \text{otherwise} \end{cases}. \tag{49}$$

The numerical discretization is summarized as the following three steps:

1. Calculate the spatial derivatives

The first-order spatial derivatives in Equation 14 can be solved by using SGPS

$$\partial_m^{\pm}\varphi = \mathrm{F}_m^{-1}\left\{ik_m e^{\pm ik_m \Delta m/2}\mathrm{F}_m\varphi\right\}(m = x\ or\ z), \tag{50}$$

where $\varphi = \left[v_x^+, v_z^+, \sigma_{xx}^-, \sigma_{zz}^-, \sigma_{xz}^-\right]$. F_m represents the 1D Fourier transform, and F_m^{-1} is the corresponding inverse transform. The $\pm$ of e-exponential denote the half spatial interval shift, where $+$ and $-$ correspond to the left (up) and the right (down) shift, respectively. The $+$ and $-$ of partial derivative φ represent the current and previous time, respectively.

2. Calculate the fractional Laplacians

$$L_\theta \frac{\partial v_m^+}{\partial n} = \rho\left\{\begin{array}{r} d_{\theta,1}\mathrm{F}^{-1}\left[k^{-1}\mathrm{F}\left(\dfrac{\partial v_m^+}{\partial n}\right)\right] + d_{\theta,2}\mathrm{F}^{-1}\left[\mathrm{F}\left(\dfrac{\partial v_m^+}{\partial n}\right)\right] + d_{\theta,3}\mathrm{F}^{-1}\left[k\mathrm{F}\left(\dfrac{\partial v_m^+}{\partial n}\right)\right] \\ +d_{\theta,4}\mathrm{F}^{-1}\left[k^{-1}\mathrm{F}\left(\dfrac{\partial}{\partial t}\dfrac{\partial v_m^+}{\partial n}\right)\right] + d_{\theta,5}\mathrm{F}^{-1}\left[\mathrm{F}\left(\dfrac{\partial}{\partial t}\dfrac{\partial v_m^+}{\partial n}\right)\right] \end{array}\right\}, \tag{51}$$

with

$$\frac{\partial}{\partial t}\frac{\partial v_m^+}{\partial n} = \frac{1}{\Delta t}\left(\frac{\partial v_m^+}{\partial n} - \frac{\partial v_m^-}{\partial n}\right)(m, n = x\ or\ z), \tag{52}$$

where F and F^{-1} represent the 2D Fourier transform and the inverse transform, respectively. The subscript $\theta = P$ or s represents P- or S-wave, respectively. The parameters of $d_{\theta,1}$ to $d_{\theta,5}$ are defined in Equation 5.

3. Update the particle velocity and stress

$$\begin{cases} v_x^+ = v_x^- + b_x \Delta t \left(\dfrac{\partial \sigma_{xx}^-}{\partial x} + \dfrac{\partial \sigma_{xz}^-}{\partial z} \right) \\ v_z^+ = v_z^- + b_z \Delta t \left(\dfrac{\partial \sigma_{xz}^-}{\partial x} + \dfrac{\partial \sigma_{zz}^-}{\partial z} \right) \\ \sigma_{xx}^+ = \sigma_{xx}^- + \Delta t \left[L_p \left(\dfrac{\partial v_x^+}{\partial x} + \dfrac{\partial v_z^+}{\partial z} \right) - 2 L_s \dfrac{\partial v_z^+}{\partial z} \right] \\ \sigma_{zz}^+ = \sigma_{zz}^- + \Delta t \left[L_p \left(\dfrac{\partial v_x^+}{\partial x} + \dfrac{\partial v_z^+}{\partial z} \right) - 2 L_s \dfrac{\partial v_x^+}{\partial x} \right] \\ \sigma_{xz}^+ = \sigma_{xz}^- + \Delta t \left[L_s{}^* \left(\dfrac{\partial v_x^+}{\partial z} + \dfrac{\partial v_z^+}{\partial x} \right) \right] \end{cases} . \tag{53}$$

In the following numerical examples, we utilize the convolutional perfectly matched layers (CPML; Komatitsch & Martin, 2007) to absorb artificial reflections.

3. Numerical Examples

3.1. Verifications of Simulation Accuracy

3.1.1. Homogeneous Model

We first solve the proposed DFL viscoelastic wave in homogeneous media and verify the accuracy by comparing the numerical result with the analytical solution. For a homogeneous medium, the analytical solution can be obtained by convolving Green's function (Nabighian, 1988) and source wavelet (Carcione, 2007). The 2D model size is 512 × 512 with a spatial interval of 10 m. The reference phase velocities are $c_p = 3.0$ km/s and $c_s = 2.0$ km/s defined at a reference frequency of 500 Hz. The time step is 1.0 ms and the density is $\rho = 2200$ kg·m^{-3}. The vertical stress source (Ricker wavelet) with a dominant frequency of 25 Hz is added. The source and receiver are located at the (256, 256) and (316, 316) grid points, respectively. In Figure 2, we show the traces of v_x component, where Figures 2a and 2b correspond to the comparison of elastic and viscoelastic ($Q_p = 32$ and $Q_s = 20$) waveforms, respectively. The red line and the black line represent the traces computed by the proposed DFL viscoelastic wave equation and the analytical solution, respectively, and the blue line displays the residuals between them. We can see that the two solutions are well-matched.

3.1.2. Decoupling of Amplitude-Loss and Phase-Dispersion

As stated above the proposed VTI-DFL viscoelastic wave equation is able to separate phase dispersion and amplitude decay effects. The decoupled formula for modeling decoupled dispersion and amplitude can be found in Appendix B. We below illustrate the decoupled effects with a numerical example. A 2D homogeneous model is discretized in 512 × 512 grids with a spatial interval of 10 m. The reference velocities defined at a high reference frequency of 500 Hz are $c_p = 2.0$ km/s and $c_s = 1.5$ km/s. The time step is 1.0 ms and the density is $\rho = 2{,}200$ kg m^{-3}. Again, we excite a vertical stress source at the center of the model, and the dominant frequency is 25 Hz. Figure 3a includes four wavefields, from left-top to right-bottom, that are, respectively, generated by the decoupled wave equations: elastic (no attenuation), the dispersion-dominated, the loss-dominated, and viscoelastic cases. Figure 3b shows the same results by considering VTI Q (where $\delta = 0.1$, $\epsilon = 0.2$, $\delta_Q = 0.2$, and $\epsilon_Q = 0.4$). In Figures 3a and 3b, we find that the wavefield generated by the loss-dominated operators has the same phase but weak amplitudes compared to the elastic wavefield; the dispersion-dominated wavefield has the uniform amplitude but visible phase delay; the viscoelastic wavefield shows both amplitude decay and the phase delay. We also show the amplitude spectra in Figures 3c and 3d and phase spectra in Figures 3e and 3f to highlight the decoupled effect. We observe that amplitude spectra of dispersion-dominated and elastic are almost identical, and loss-dominated and viscoelastic show smaller amplitude. In Figures 3e and 3f, good agreement of phase spectra between red (loss-dominated) and black (elastic) lines, blue (viscoelastic), and green lines (dispersion-dominated) can also be observed.

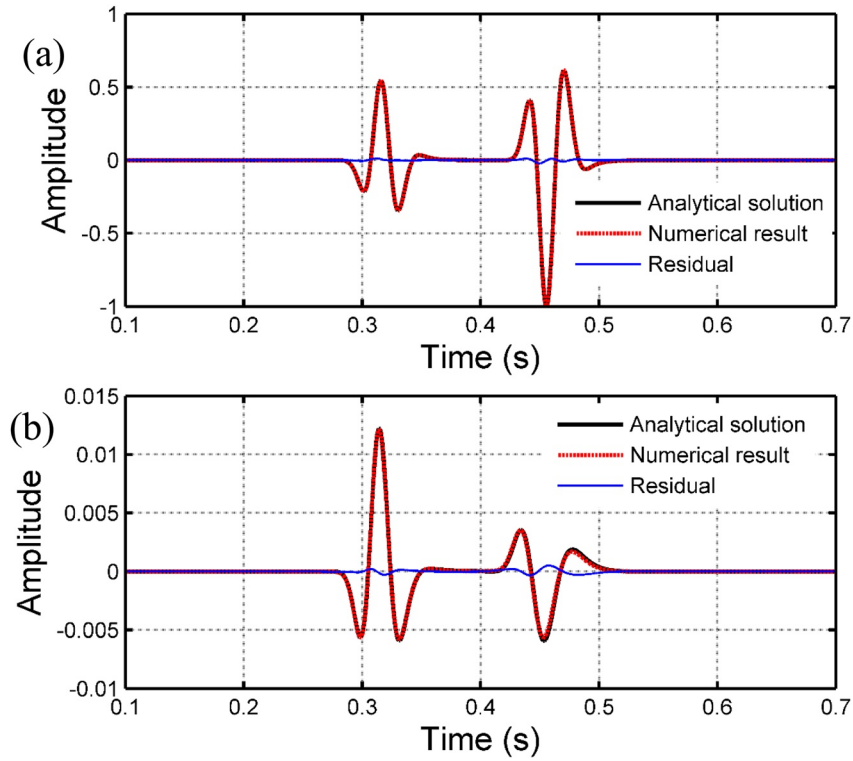

Figure 2. Comparison of seismograms computed by numerical (red dashed lines), analytical synthetic (black solid lines), and their waveform residual (blue solid lines) in (a) the elastic media and (b) the viscoelastic media.

3.1.3. Two-Layer Model

The proposed DFL viscoelastic wave equation is free of the mixed-domain problem, thus naturally adapts to heterogeneous attenuation models. This superiority is demonstrated below. Figure 4a shows three two-layer models: (a) varying velocities and a homogeneous Q; (b) a homogeneous velocity and varying Q; (c) varying velocities and Q. Each model is discretized into an 800×800 grid with 10 m spatial interval. A horizontal interface exists at depth of 4.4 km. A Ricker wavelet source is located at the center of the model with a dominant frequency of 25 Hz. The time step is 1.0 ms. Here, we use three approaches to perform simulation: the average γ scheme of Zhu and Harris (2014); the proposed DFL viscoelastic wave equation; a reference (accurate) solution created by pointwise FFT scheme (Chen et al., 2016) where fractional Laplacians are computed independently for the top and bottom layers. Figure 4b displays the snapshots at 1.0 s, where the first column shows the reference solution, the second column highlights the residual between the reference and the average scheme, and the third column shows the residual between the reference and the new DFL viscoelastic wave equation. In Model 1, since the Q model is homogeneous, the wavefield by the average scheme is identical to the reference one. Nevertheless, with the varying Q (Model 2 and Model 3), the wavefield differences between two schemes are very clear. The third column in Figure 4b exhibits only subtle residuals, which verifies the capability of our new scheme to handle heterogeneous attenuation media.

3.2. Verifications of Simulating Q Anisotropy

3.2.1. Homogeneous Model

This section designs a set of anisotropic homogeneous models to verify the accuracy of the attenuation anisotropy simulated by the proposed VTI-DFL viscoelastic wave equation. These models select a range of anisotropic Q values to represent weak to strong anisotropy. Table 1 lists different attenuation anisotropy parameters of ϵ_Q and δ_Q. The testing models contain 800×800 grid points with a uniform grid spacing of 10 m. We use a time step of 1.0 ms. The anisotropic elastic parameters are $c_p = 3.0$ km/s, $c_s = 1.5$ km/s, $\rho = 2{,}000$ kg m^{-3}, Thomsen's parameters $\epsilon = 0.16$ and $\delta = 0.1$. Figure 5 shows the circle acquisition geometry (receivers are represented by

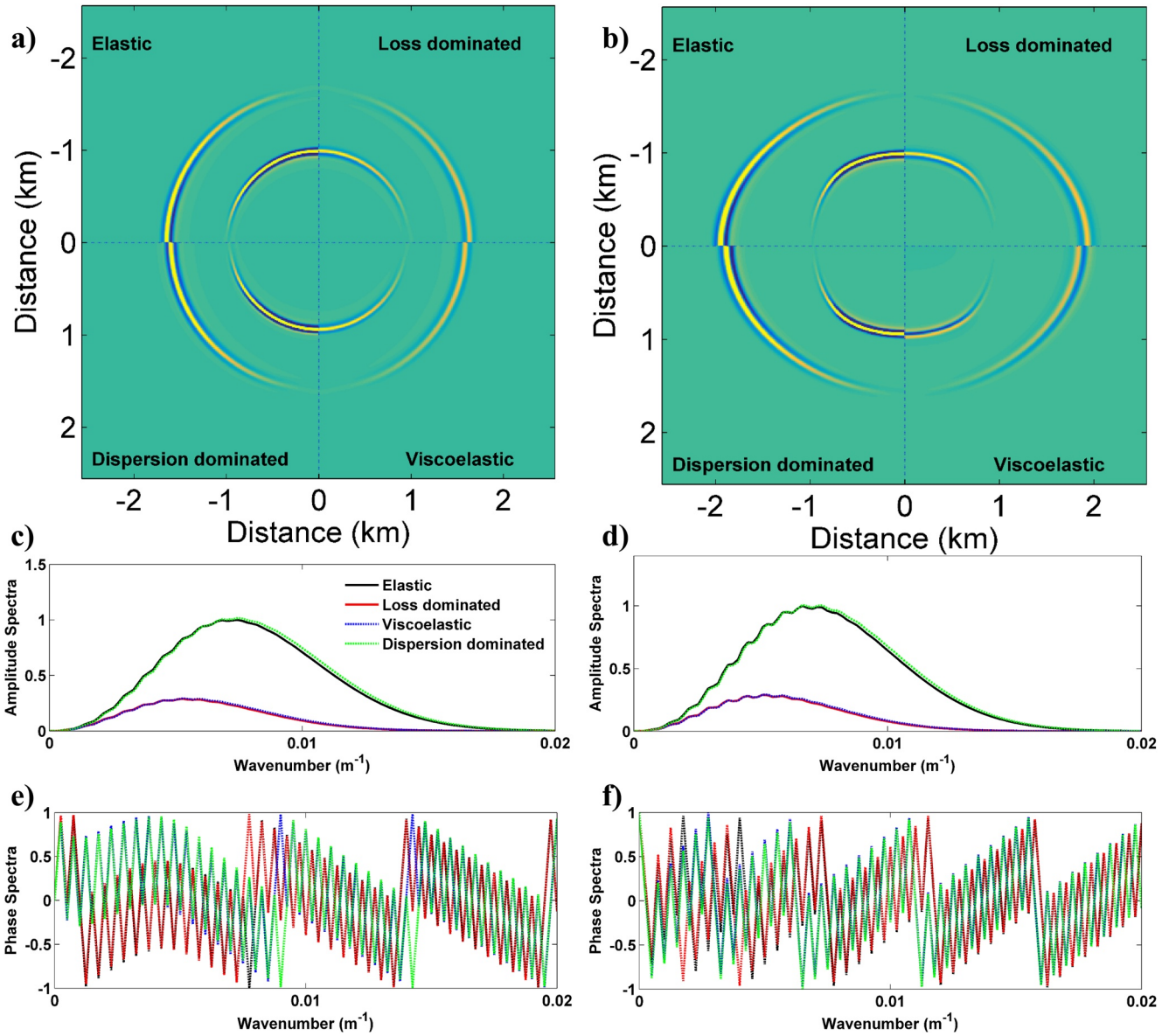

Figure 3. Decoupled phase dispersion and amplitude loss of the proposed DFL and VTI-DFL viscoelastic wave equations. In (a) and (b), four wavefields (separated by dashed lines) from left-top to right-bottom are, respectively, generated by the decoupled wave equations: elastic (no attenuation), the dispersion-dominated, the loss-dominated, and viscoelastic cases. (c) and (d) show amplitude spectra, and (e) and (f) phase spectra.

triangles and uniformly distributed at every 1°). The red star represents a Ricker wavelet with 25 Hz dominant frequency. Figure 6 displays the shot gathers of v_x component, in which the left and right columns correspond to the inner receiver array and the outer receiver array, respectively. Comparing the left and the right columns, the seismograms of the outer receivers show obvious late arrival of P- and S-waves. Moreover, the significant difference between seismograms of different models reflects the variation of attenuation anisotropy parameters.

Then, we use the spectral ratio method (Aki, 1980) to estimate Q values. The amplitude spectrum of left and right columns in Figure 6 are $R_1(f)$ and $R_2(f)$, respectively. Defining the logarithm of $\frac{R_1(f)}{R_2(f)}$ as $L(f)$, we have

$$L(f) = \ln\frac{R_1(f)}{R_2(f)} = \ln\frac{G_1}{G_2} - \frac{\pi\Delta t}{Q}f, \tag{54}$$

where G_1 and G_2 represent the geometric spreading factors for two sets of receivers, Δt is the time interval between inner seismogram and outer seismogram. $L(f)$ is a linear function with intercept $\ln(G_1/G_2)$ and slope

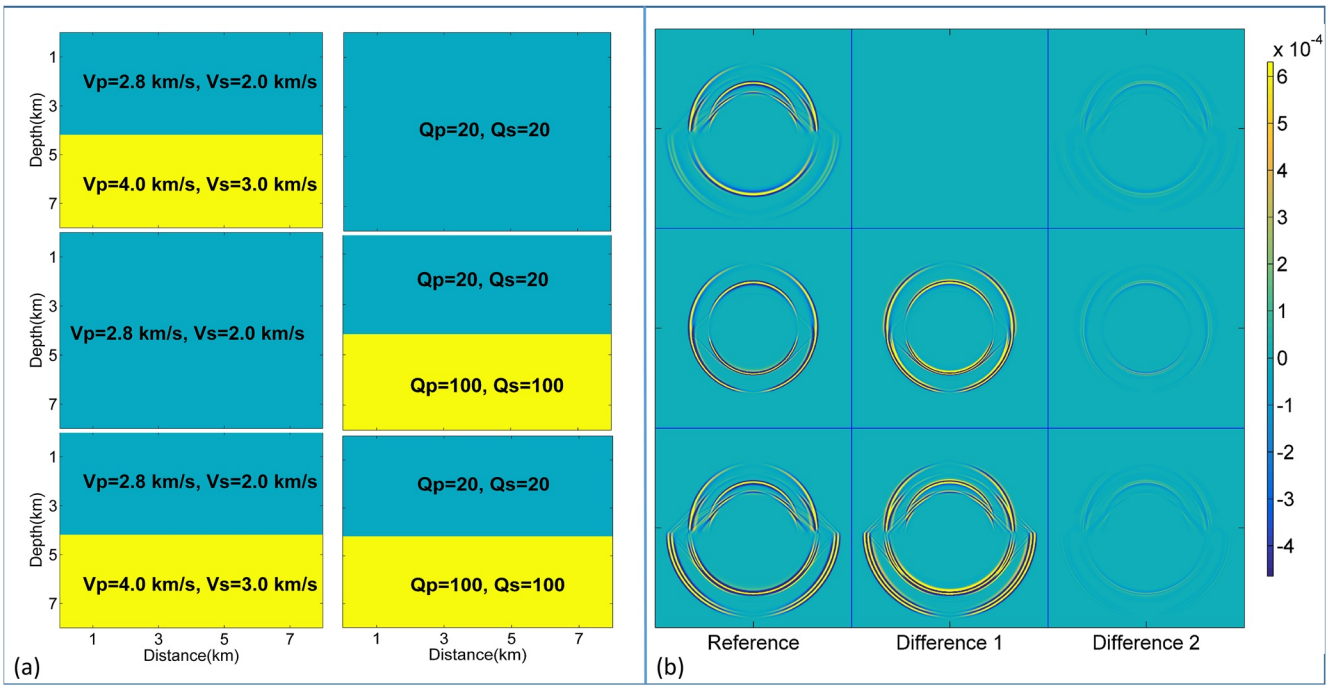

Figure 4. (a) A set of two-layer models, the left column is velocity, and the right column represents Q models, respectively. (b) Wavefield snapshots at 1.0 s. The reference is calculated by the pointwise FFT scheme; Residual one is the difference between the wavefield solved by the average scheme and the reference; Residual two is the difference between the wavefield computed by our DFL viscoelastic wave equation and the reference.

$k = -\pi\Delta t/Q$. Thus, we estimate quality factors by $Q = -\pi\Delta t/k$. It should be mentioned that since both P- and S- waveforms are included in Figure 6, we window out each waveform and estimate Q_P and Q_S separately. We compare dissipation factors $1/Q_p$ and $1/Q_s$ in Figures 7a and 7b, where solid lines represent the theoretical values obtained by solving the Christoffel equation (see Appendix C) and circles denote the numerical values estimated using the spectral ratio method. We can see that the accuracy of numerical Q values can be divided into two scenarios: Models 1–4 are well matched for both Q_P and Q_S; for Models 5–7, Q_P deviation appears when δ_Q is bigger, but the accuracy of Q_s is still satisfied even for the extreme case ($\delta_Q = -1.68$). We conclude that the proposed VTI-DFL viscoelastic wave equation can accurately describe the direction-dependent attenuation over a wide range of anisotropy.

3.2.2. Influence of Attenuation Anisotropy on the Waveform

To investigate the influence of attenuation anisotropy on the waveform, we set the velocity to be isotropic, and only consider the attenuation anisotropy (parameters are listed in Table 2). Model 1 presents isotropic attenuation as a reference. Model 2 and Model 3 are used to investigate the influence of ϵ_Q, while Model 4 and Model 5 will highlight the influence of δ_Q. In Figure 8, the left and right columns represent theoretical Q_p and Q_s predicted using the Zhu-Tsvankin definition (Zhu & Tsvankin, 2006), where the black, red, blue, green, and purple curves correspond to Model 1 to Model 5, respectively. From Figure 8a, we can see that ϵ_Q predominantly affects P-wave attenuation in the horizontal direction: the attenuation increases monotonically when ϵ_Q increases from −0.5 to 0.5. Similarly, a larger δ_Q causes a stronger attenuation, but the influence of δ_Q on P-wave attenuation is mainly reflected in the non-axial direction shown in Figure 8c. In Figures 8b and 8d, we find that S-wave attenuation mainly depends on the magnitude relationship between ϵ_Q and δ_Q: the non-axial attenuation becomes stronger when $\epsilon_Q > \delta_Q$, and vice versa.

Below we show simulated wavefields in Figures 9a–9e for all models in Table 2. Figures 9f–9i represent the wavefield residuals between Figures 9b–9e and 9 (the isotropic attenuation case). Similar observations

Table 1
Anisotropic Q_{ij} Properties of Seven 2D TI Homogeneous Models

Testing models	Q_{11}	Q_{13}	Q_{33}	Q_{55}	ϵ_Q	δ_Q
Model 1	20	30	20	15	0.00	0.00
Model 2	35	50	50	30	0.43	0.75
Model 3	50	40	25	20	−0.50	−0.22
Model 4	80	20	20	15	−0.75	−0.40
Model 5	50	68	35	60	−0.30	−0.90
Model 6	50	40	25	60	−0.50	−1.16
Model 7	50	40	15	60	−0.70	−1.68

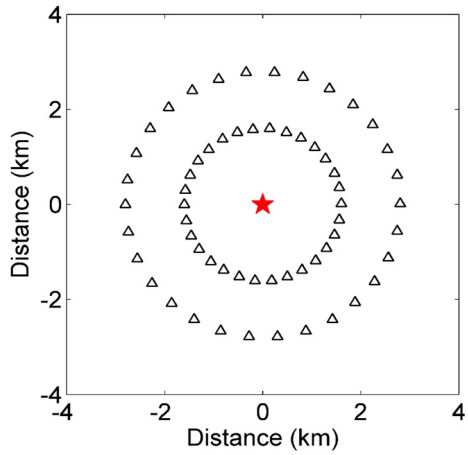

Figure 5. Verification experiment: circle acquisition system for estimating anisotropic Q by the spectral ratio method. A red star marks the source, and 720 receivers are represented by triangles. Note that every 10th receiver is shown.

of the anisotropy impact on the waveform can be drawn from Figure 9: (1) when $\varepsilon_Q \neq 0$ and $\delta_Q = 0$ (Model 2 and Model 3), the difference of P-wave is mainly seen in the horizontal direction in Figures 9h and 9i; when $\varepsilon_Q = 0$ and $\delta_Q \neq 0$ (Model 4 and Model 5), the difference of P-wave is mainly seen in the non-axial direction in Figures 9h and 9i; (2) For all models the difference of S-wave is mainly seen in the non-axial direction in Figures 9f–9i.

3.2.3. Complex Heterogeneous Model

Next, we demonstrate the numerical implementation of the proposed VTI-DFL viscoelastic wave equation in the complex heterogeneous media using the industrial standard BP velocity anisotropic model. Figures 10a–10d correspond to P-wave velocity, quality factor Q_p, Thomsen's parameters of δ and ε, respectively. The S-wave velocity and quality factor Q_s are empirically obtained by $c_s = c_p/1.73$, and $Q_s = Q_p/1.2$. The anisotropic attenuation parameters are transformed by $\delta_Q = 2\delta$, and $\varepsilon_Q = 3\varepsilon$. The model contains 500×270 grid points with a spacing of 10 m. An explosive source is added at (2500 m, 30 m), and the receivers are located at 50 m depth. The dominant frequency of the source is 25 Hz. The simulation time is 2.5 s with a time step of 1.0 ms. To verify the simulation accuracy, the existing VTI-TF viscoelastic wave equation (Zhu, 2017) acts as a reference solution.

Figure 11 shows wavefield snapshots and common shot gathers of a horizontal particle velocity v_x component. From top to bottom, they are corresponding to results from the proposed VTI-DFL viscoelastic wave equation, the VTI-TF viscoelastic wave equation, and the difference between VTI-DFL and VTI-TF viscoelastic wave equations, respectively. It can be found that the VTI-DFL and VTI-TF viscoelastic wave equations simulate matched wavefields and common shot gathers with minor differences (see Figures 11e and 11f). Wavefields in Figures 12a–12c correspond to the non-attenuated, the anisotropic attenuated, the isotropic attenuated cases. Compared to reference elastic wavefield (Figure 12a), it is not surprising that the attenuation significantly reduces the amplitude (see Figures 12b and 12c). Visible waveform residual between isotropic attenuation and anisotropic attenuation (see Figure 12d) reflect the effect of Q anisotropy on wavefields. Figure 13 displays seismograms recorded at (2,000 m, 30 m) for a detailed comparison. The well-matched seismograms (black and red lines) certify the accuracy of the VTI-DFL viscoelastic wave equation. The insert plot in Figure 13b is to highlight the difference between isotropy (red) and anisotropy (blue), implying that attenuation anisotropy affects both phase and amplitude.

3.3. Application to the Salton Trough Model

We finally choose the 3D Salton Trough model, shown in Figure 14a, to demonstrate the generalization and feasibility of the proposed VTI-DFL viscoelastic wave equation for simulating wave propagation on the crustal-scale. The simulated area includes the Coachella Valley with the San Andreas fault located on its northeast flank. The original 3D P-wave velocity model inverted by Ajala et al. (2019) contains 19 grids within the depth from 0 to 9 km, 101 grids in longitude from 115.7°W to 116.7°W, and 91 grids in latitude from 33.3°N to 34.2°N. Since the original data points are not uniformly distributed, we perform a linear interpolation and resampling to obtain a new P-wave velocity model in $505 \times 455 \times 48$ grid points with spacing of 200 m in Figure 14b. Figures 14c and 14d show 2D P-wave velocity profiles at different latitudes and longitudes, and the S-wave velocity c_s is empirically obtained by $c_s = c_p/1.73$. Lateral seismic velocity contrasts are strong at the surface, and a low-velocity region is visible on the eastern side of the Coachella Valley near the San Andreas fault. We estimate Q model from the P-wave velocity model with an empirical formula: $Q_p = Q_s = 3.516(c_p/1000)^{2.2}$ (Li, 1993); thus, the low-velocity region also shows high attenuation. In addition, we set homogeneous anisotropic parameters of $\delta = 0.05$, $\varepsilon = 0.1$, $\gamma = 0.1$, $\delta_Q = 0.1$, $\gamma_Q = 0.2$, and $\varepsilon_Q = 0.2$.

A vertical stress point source with a dominant frequency of 5 Hz is located at the spot (50 km, 46 km, 1.6 km), and the receivers are placed at all grid points of the x-y plane at the surface. The free-surface boundary at the top is realized by vacuum formalism (Zahradník et al., 1993); specifically, the density above the surface is set to zero and the velocities close to zero (to avoid division by zero) to approximate a vacuum. On other edges of the

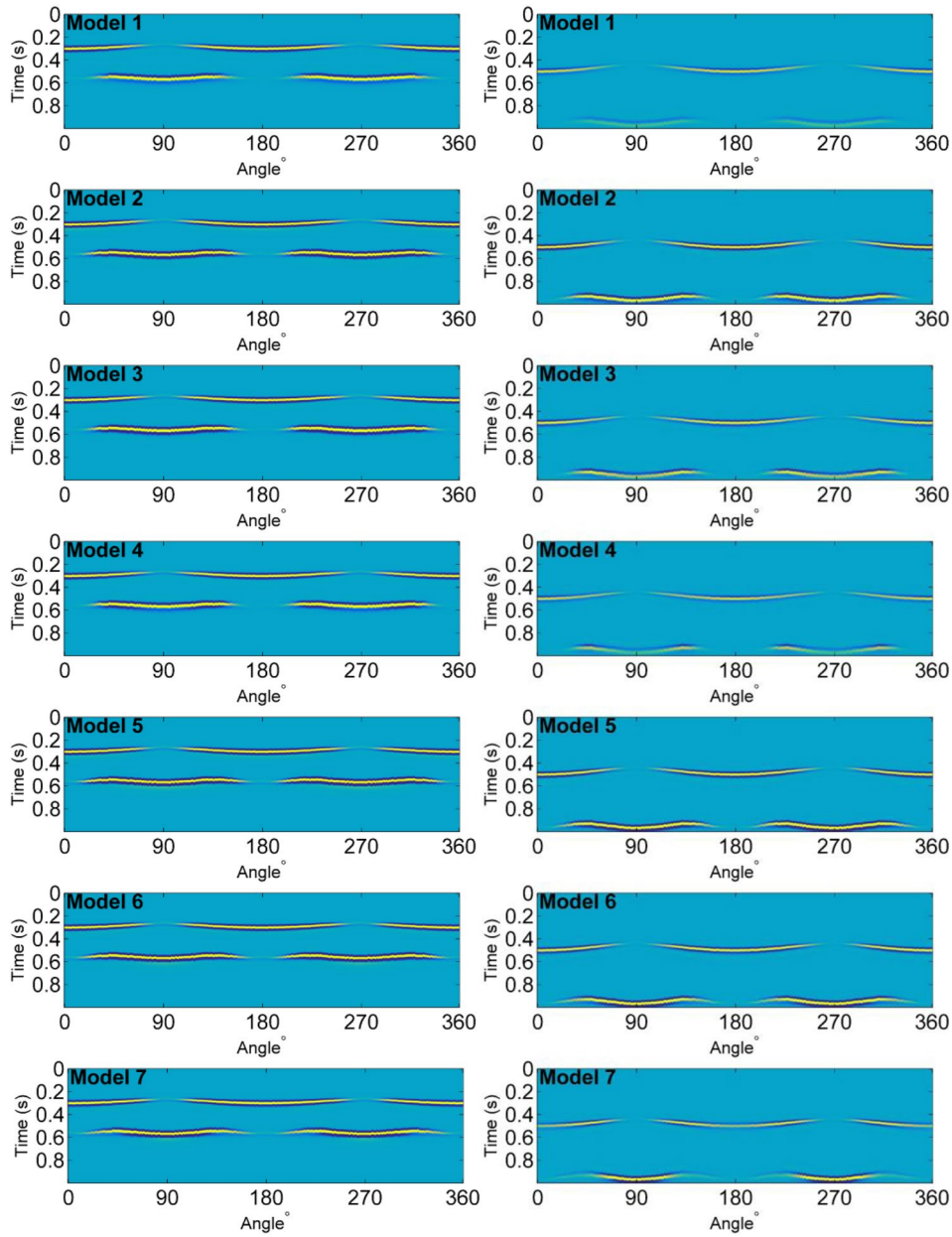

Figure 6. Simulated seismograms of v_x component, where the left and right columns correspond to the receivers at inner and outer concentric circles in Figure 5, respectively.

computational domain, we add the CPML to absorb artificial reflections. The simulation time lasts 15 s with a time step of 5.0 ms. Wavefield snapshots of v_x component at different times simulated by the proposed VTI-DFL viscoelastic wave equation are displayed in Figure 15, where red and blue denote the positive and negative values, respectively. After a propagation time of 7.5 s, we observe trapped seismic waves along the San Andreas fault and possible scattering energy around (marked by arrows). Along the fault, seismic waves propagate slower than in the surrounding areas. Meanwhile, significant amplitude decay of seismic waves in the Coachella Valley (marked by ellipses) is caused by high attenuation.

To evaluate the accuracy of the proposed VTI-DFL viscoelastic wave equation on the 3D Salton Trough model, we compute the reference waveform from a VTI-TF viscoelastic wave equation (Zhu, 2017). Because the VTI-TF viscoelastic wave equation requires substantial computer memory, to enable the time-fractional simulation to be feasible, we downsample the model by two in each direction to 252 × 227 × 24 grid points with a spacing

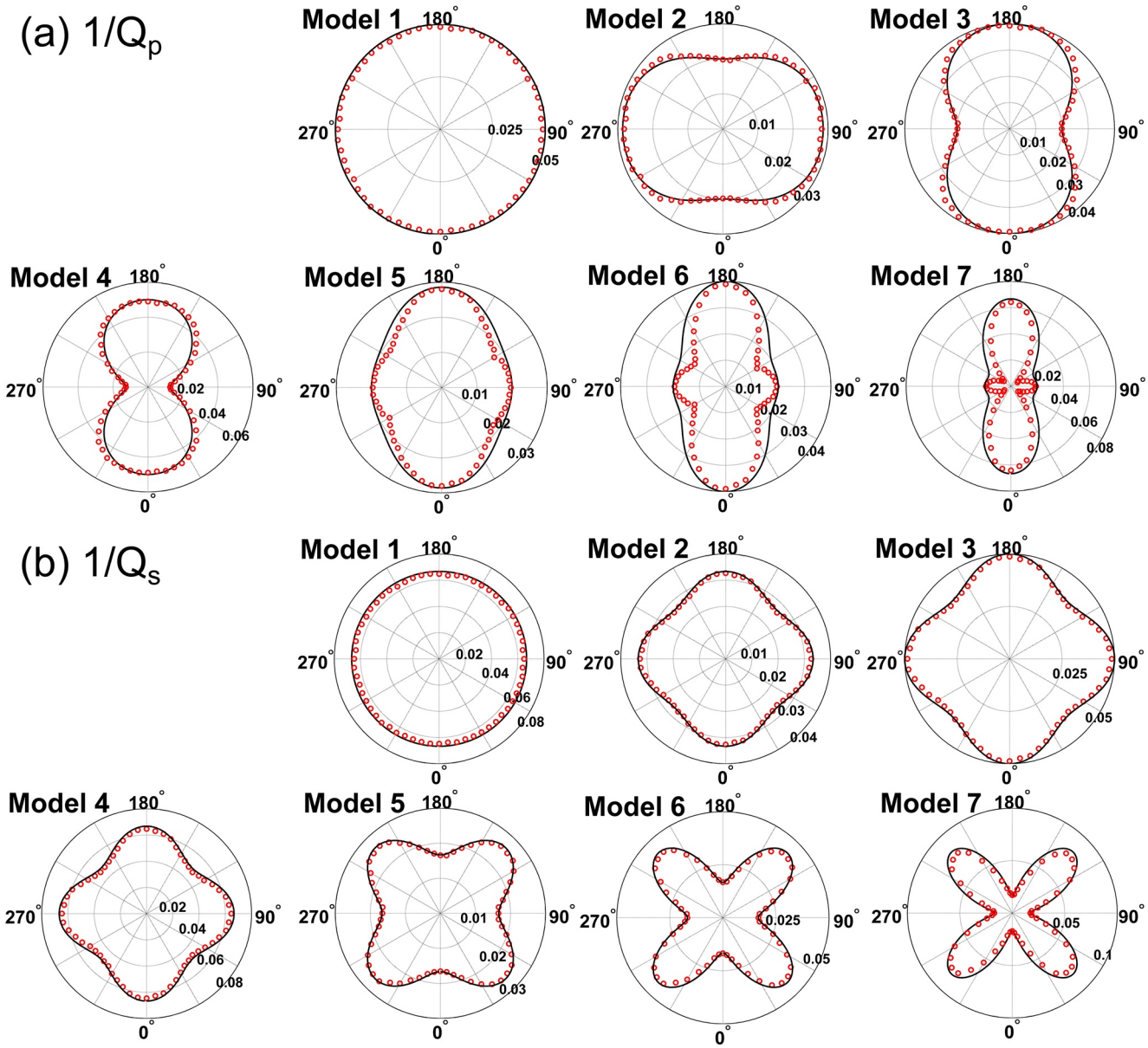

Figure 7. Comparisons of the anisotropic dissipation factors (a) and (b). The solid lines represent theoretical values computed by the Christoffel equation, and the red circles denote numerical values estimated from the spectral ratio method.

Table 2
A Group of Models Designed to Analyze the Effects of Anisotropic Attenuation Parameters on the Waveforms

Testing models	Q_{33}	Q_{55}	ε_Q	δ_Q
Model 1	25	20	0	0
Model 2	25	20	−0.5	0
Model 3	25	20	0.5	0
Model 4	25	20	0	−0.5
Model 5	25	20	0	0.5

of 20 m. The source dominant frequency is increased to 25 Hz and the time step is reduced to 1.0 ms. We utilize the CPML at all boundaries to absorb artificial reflections. Figure 16 shows 3D common shot gathers of v_x component, in which we show the snapshot at 1.5 s on a horizontal slice and display common shot gathers at the x- and y-directions on two vertical profiles. Figures 16a–16c are calculated by the proposed VTI-DFL method, the existing VTI-TF scheme, and the VTI elastic wave equation, respectively. We find that Figures 16a and 16b are very similar and their amplitudes are significantly weaker than Figure 16c due to high attenuation. Quantitatively, we evaluate the similarity of waveforms from two numerical schemes using the time-frequency envelope misfit (TFEM) and time-frequency phase misfit (TFPM, Kristekova et al., 2006; 2009) in Figure 17. We find well-matched

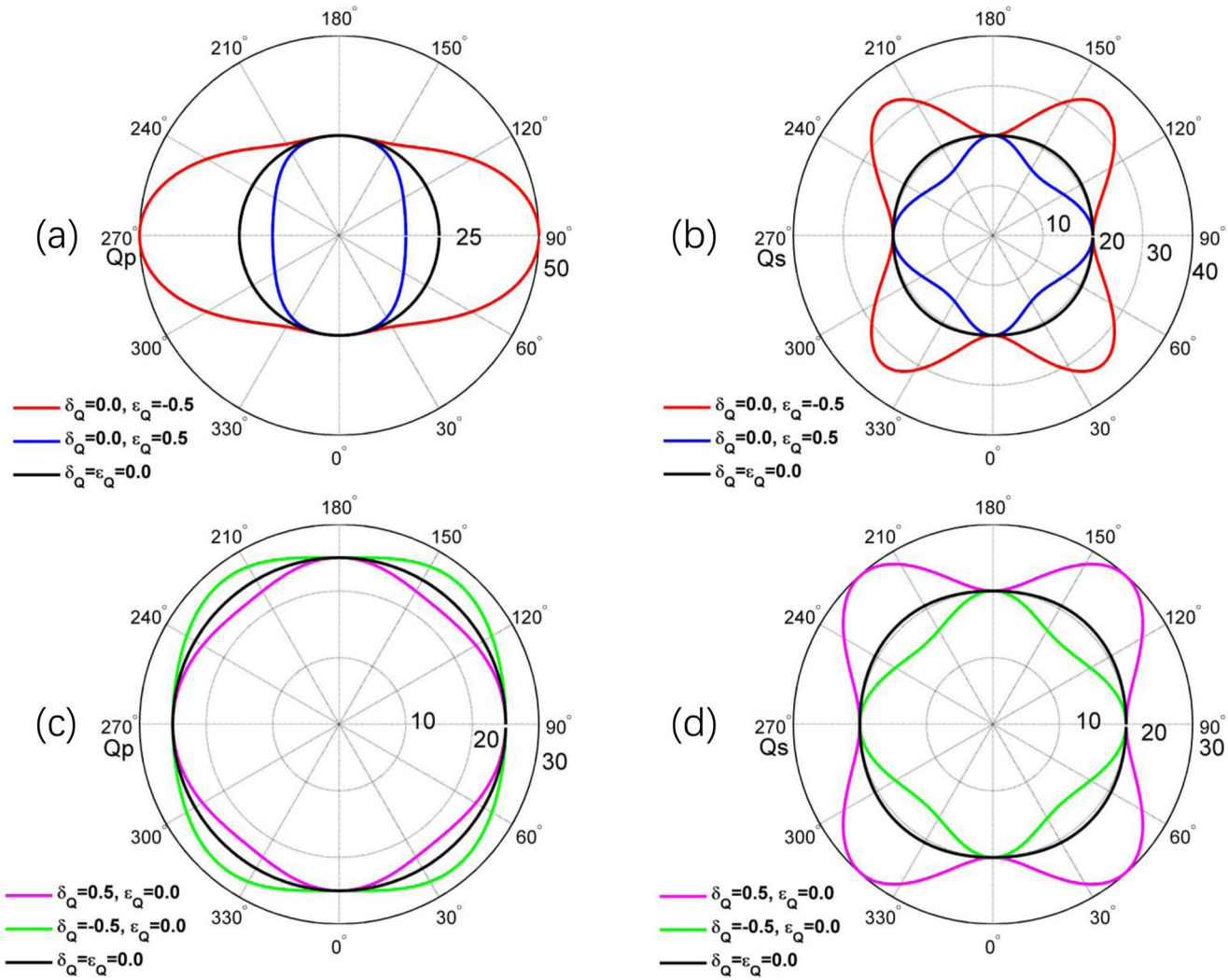

Figure 8. Theoretical values (left column) and values obtained by solving the Christoffel equation (right column). The black, red, blue, green, and purple curves correspond to Model 1 to Model 5 in Table 2.

seismograms for all three components, and the TFEM and TFPM are within 2%, which indicates the seismograms generated by the proposed VTI-DFL viscoelastic wave equation are almost identical to the reference waveforms.

4. Discussion

In Table 3, we list the detailed computation time of the 2D BP model and the 3D Salton Trough model. The Matlab codes are run on a Linux workstation (Intel Xeon CPU v4, 3.00 GHz, 256 GB RAM). Compared to the proposed DFL or VTI-DFL viscoelastic wave equations, the numerical implementation of the time-fractional viscoelastic wave equation (e.g., Zhu, 2017) is much more expensive (about 70 times slower) due to its miscellaneous intermediate variables and heavy I/O operation. We further simulate DFL viscoelastic wave equation using CUDA programming on a RTX 2080 GPU (8 GB memory), and the computational efficiency is further significantly improved (about 500 times faster) due to the powerful multi-core advantage of GPU. In contrast, solving the time-fractional equation due to its huge memory requirement cannot be implemented in the limited-memory GPU card at this moment. We conclude that, compared to the time-fractional viscoelastic wave equation, the proposed DFL viscoelastic wave equation enjoys a great advantage in the computational efficiency for exploration and regional seismic scales.

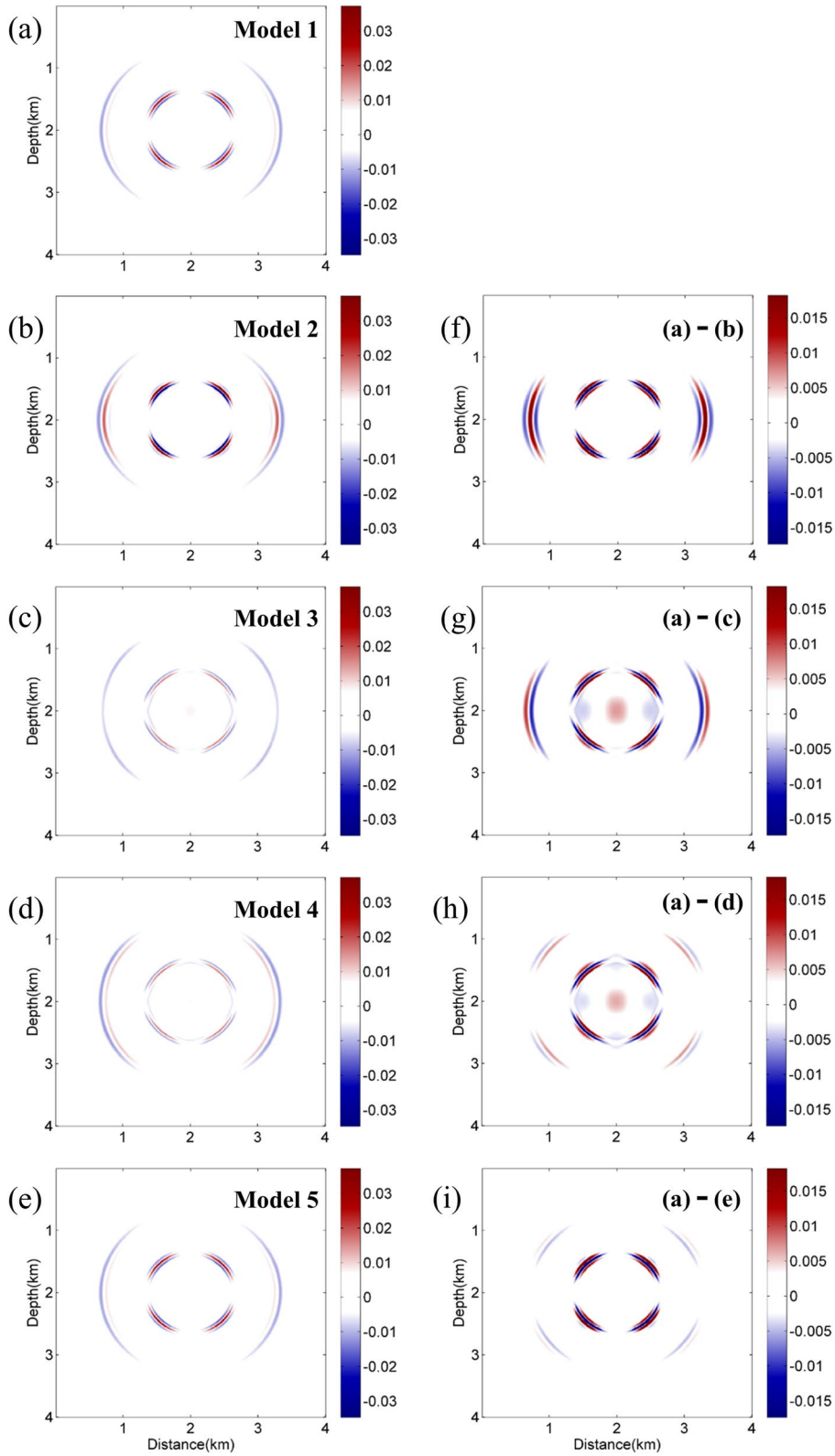

Figure 9. (a)–(e) Snapshots generated by the proposed VTI-DFL viscoelastic wave equation for all five models listed in Table 2. (f)–(i) represent the differences between (b)–(e) with (a), respectively.

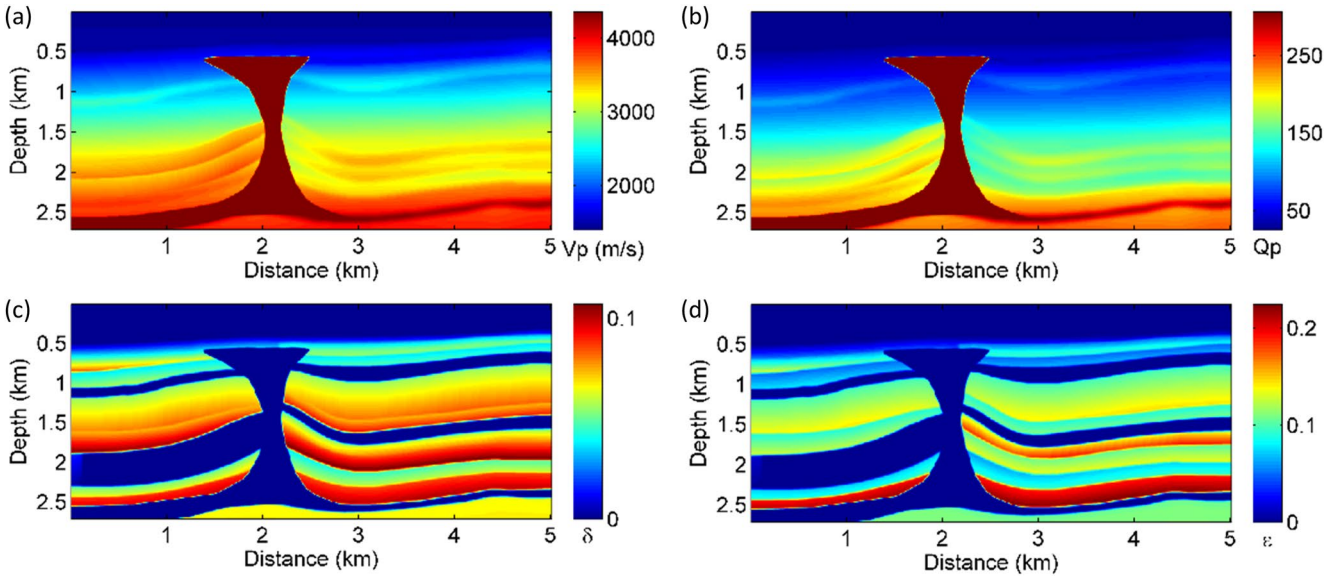

Figure 10. 2007 BP VTI model: (a) P-wave velocity, (b) P-wave quality factor, (c) Thomsen parameter δ, (d) Thomsen parameter ε.

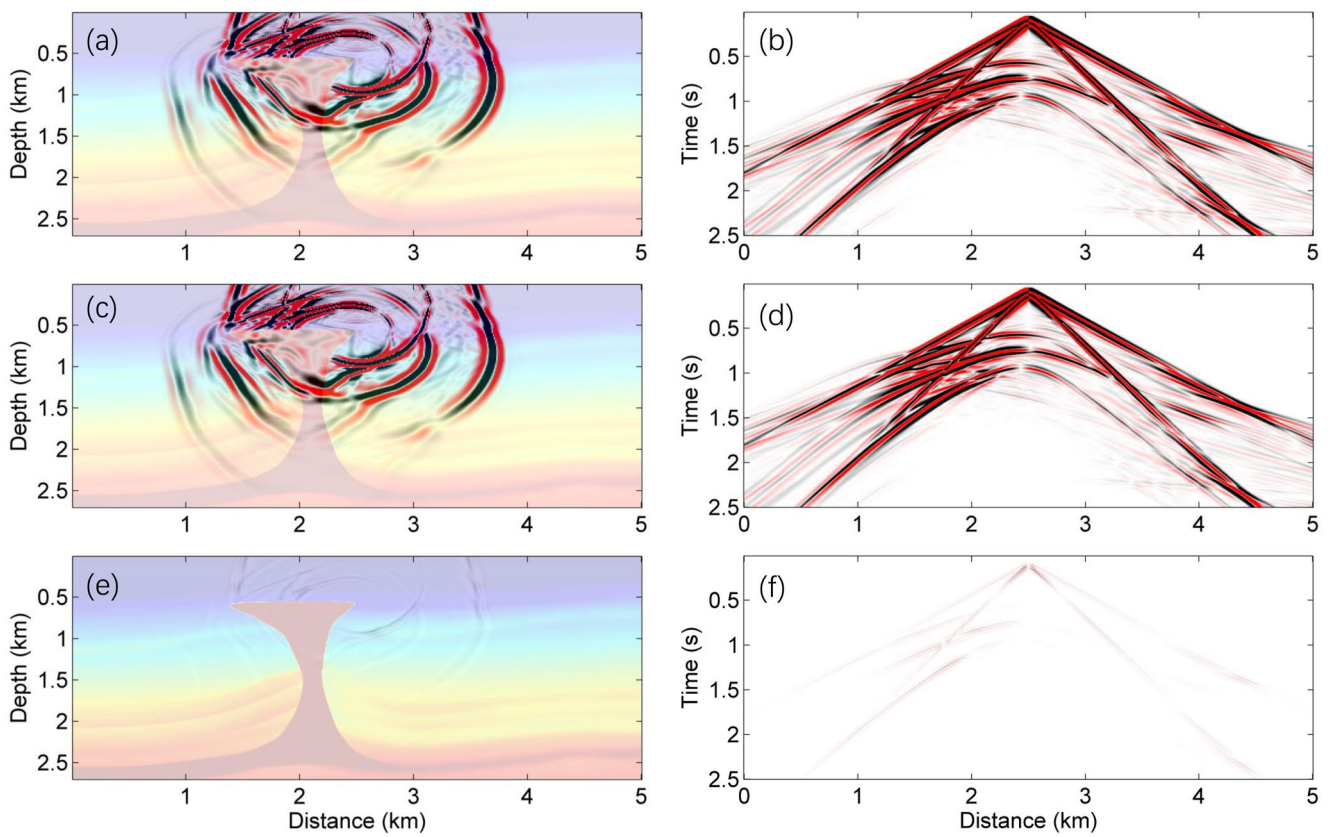

Figure 11. Wavefield snapshots at 1.8 s (left column) and common shot gathers (right column) that generated by solving (a) and (b) the proposed VTI-DFL viscoelastic wave equation, (c) and (d) existing VTI-TF viscoelastic wave equation. (e) represents the residual between (a) and (c), and (f) represents the residual between (b) and (d).

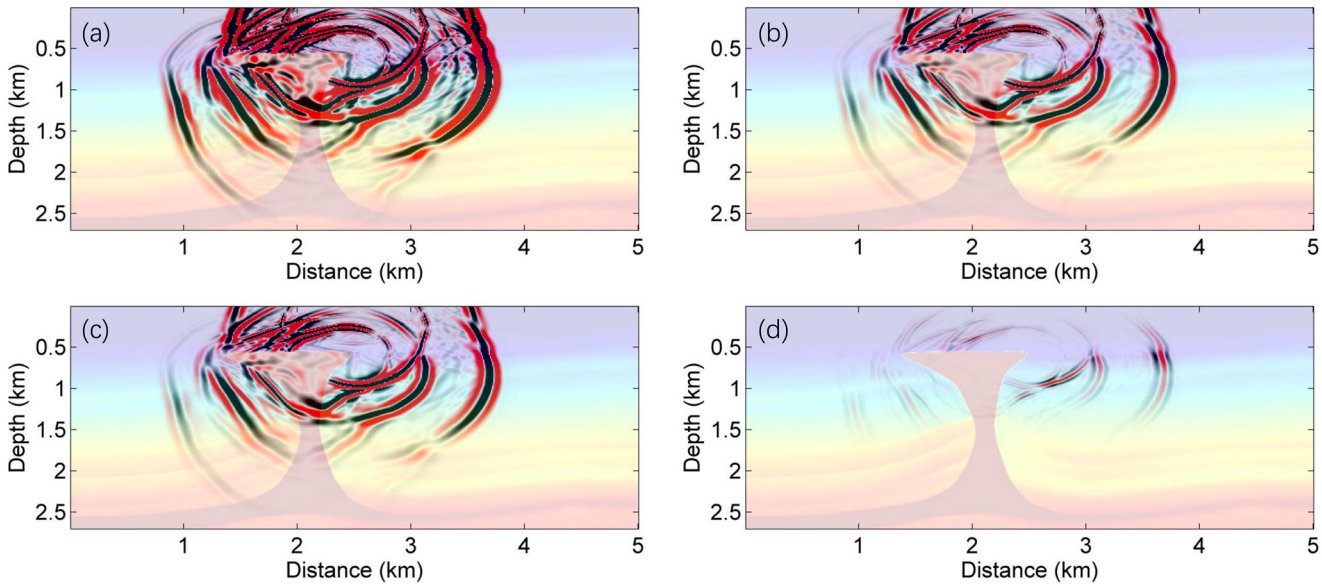

Figure 12. Wavefield snapshots with (a) no attenuation, (b) anisotropic attenuation, (c) isotropic attenuation. (d) represents the residual between (b) and (c). All snapshots in Figures 11 and Figure 12 are shown under the same colorscale.

In this study, we did not attempt to modeling the surface waves with topography because the DFL/VTI-DFL wave equations are commonly computed by the pseudo-spectral method, which requires a uniform sampling. To simulate surface wave propagation with topography, solving the DFL/VTI-DFL wave equations by non-uniform FFTs (NUFFT; Lee & Greengard, 2005) is a potential approach but needs further research.

5. Conclusions

Starting from the frequency-independent Q model, we derived a VTI viscoelastic wave equation using spatially-independent-order fractional Laplacians. The proposed equation is attractive because of these following features: first, it has the ability to model seismic anisotropy (VTI) of velocity and attenuation simultaneously; second, this wave equation is able to decouple the amplitude decay and the phase dispersion; third, the developed spatially-independent-order DFLs can naturally adapt to complex heterogeneous media; fourth, different from the conventional anelastic modeling (e.g., GSLS and fractional time derivative methods), the proposed scheme contains spatial fractional Laplacians thus exempts from the memory issue. The accuracy of the DFL viscoelastic wave equation is verified by matching the analytical solution in homogeneous media; its ability to deal with heterogeneous media is further verified by numerical tests of the two-layer model. For the VTI-DFL viscoelastic wave equation, the ability to describe the attenuation anisotropy is demonstrated by a set of homogeneous models that the attenuation anisotropy parameters vary over a wide range. We show the applications in the crustal-scale seismic modeling including BP anisotropic seismic model and the 3D Salton Trough model. Moreover, we show the computational efficiency of the proposed VTI-DFL viscoelastic wave equation over the traditional time-fractional wave equation. We anticipate that the proposed VTI-DFL viscoelastic wave equation is able to benefit seismic simulation and imaging practice as well as the development of Q-FWI.

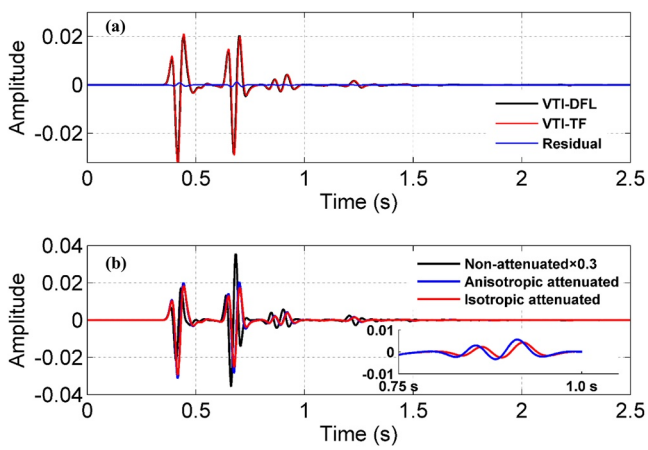

Figure 13. Seismograms recorded at (2000 m, 30 m) computed by (a) VTI-DFL and VTI-TF viscoelastic wave equations; (b) seismograms comparison between non-attenuated, the anisotropic attenuated, and the isotropic attenuated cases.

Appendix A: Three-Dimensional DFL and VTI-DFL Viscoelastic Wave Equations

The three-dimensional spatially independent-order DFL viscoelastic wave equation in the first-order form is

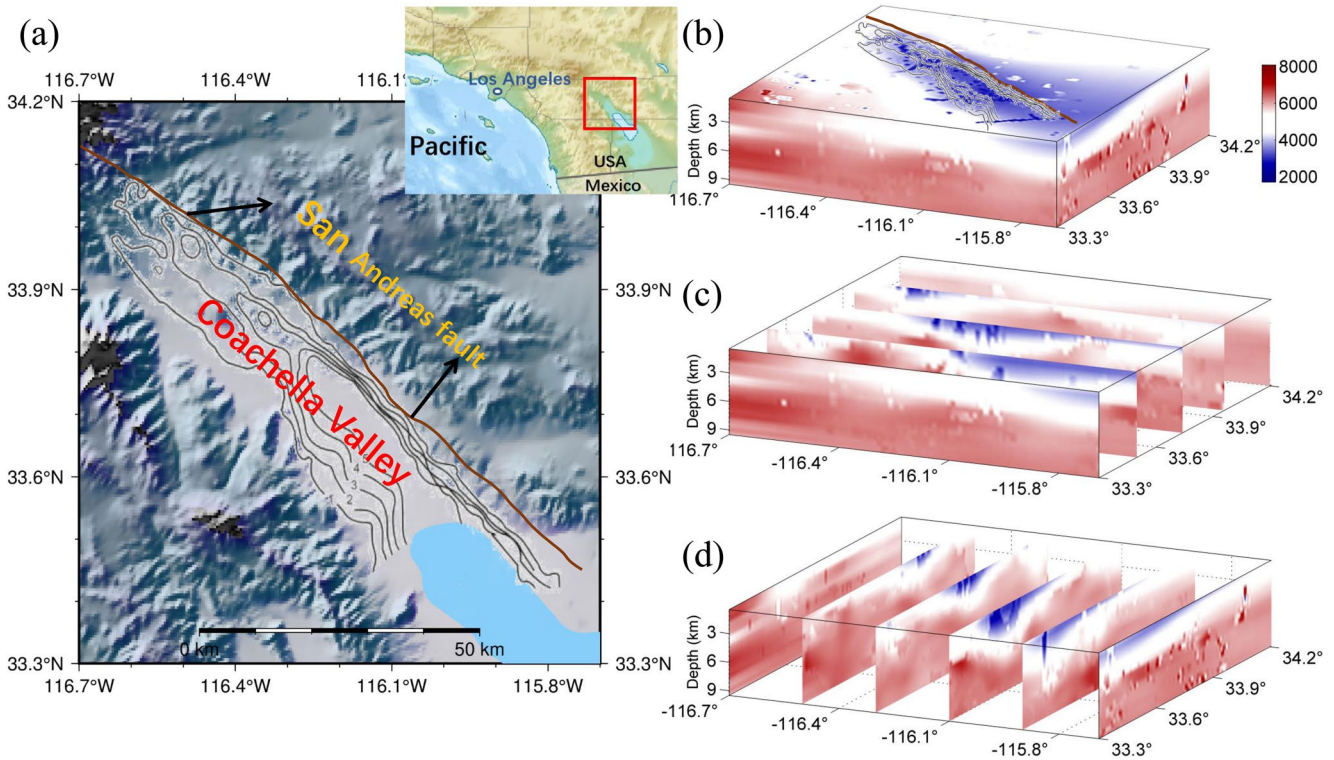

Figure 14. (a) Map of the Salton Trough, (b) 3D P-wave velocity model with a low velocity (high attenuation) region at the eastern side of Coachella Valley near the San Andreas fault (red curve); velocity profiles at four different cross-sections along (c) latitude and (d) longitude.

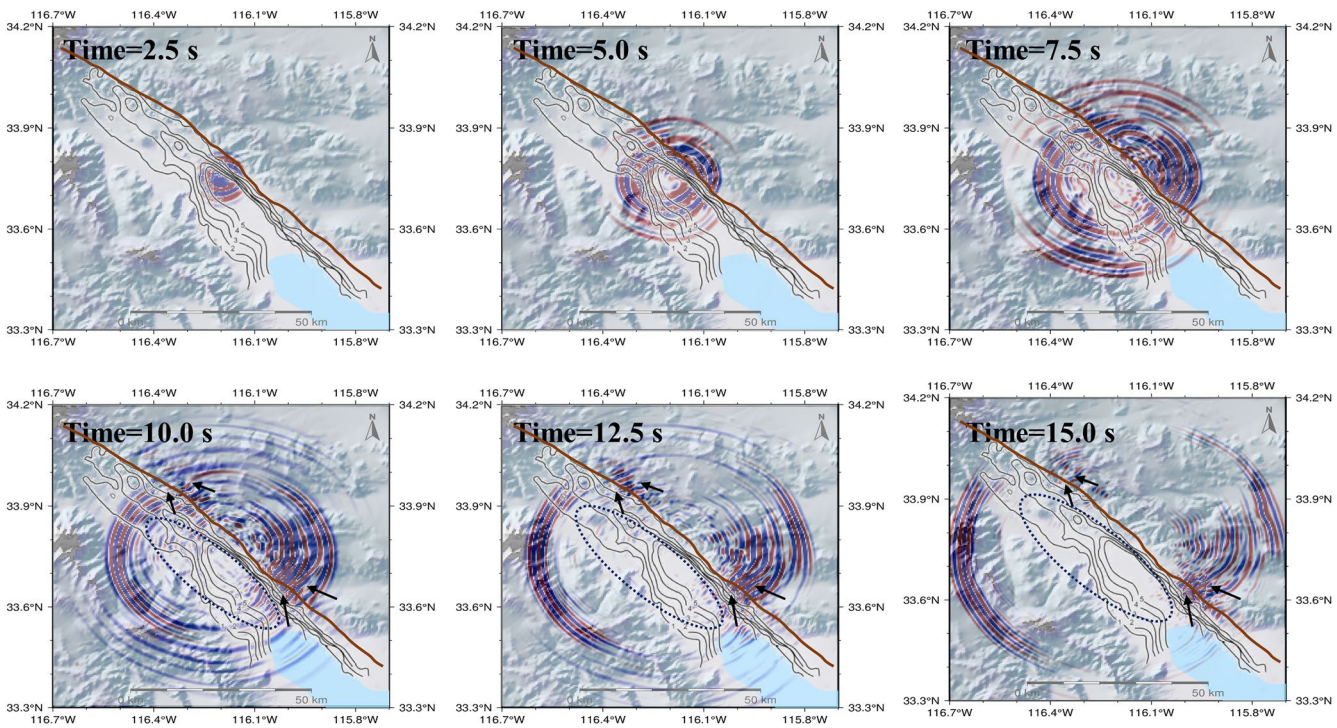

Figure 15. Wavefield snapshots calculated by the proposed VTI-DFL viscoelastic wave equation at different times. After 7.5 s, significant amplitude decay occurs in the Coachella Valley (marked by ellipses) due to high attenuation; seismic waves are trapped around the San Andreas fault (marked by arrows), and along the fault propagate slower than in the surrounding areas.

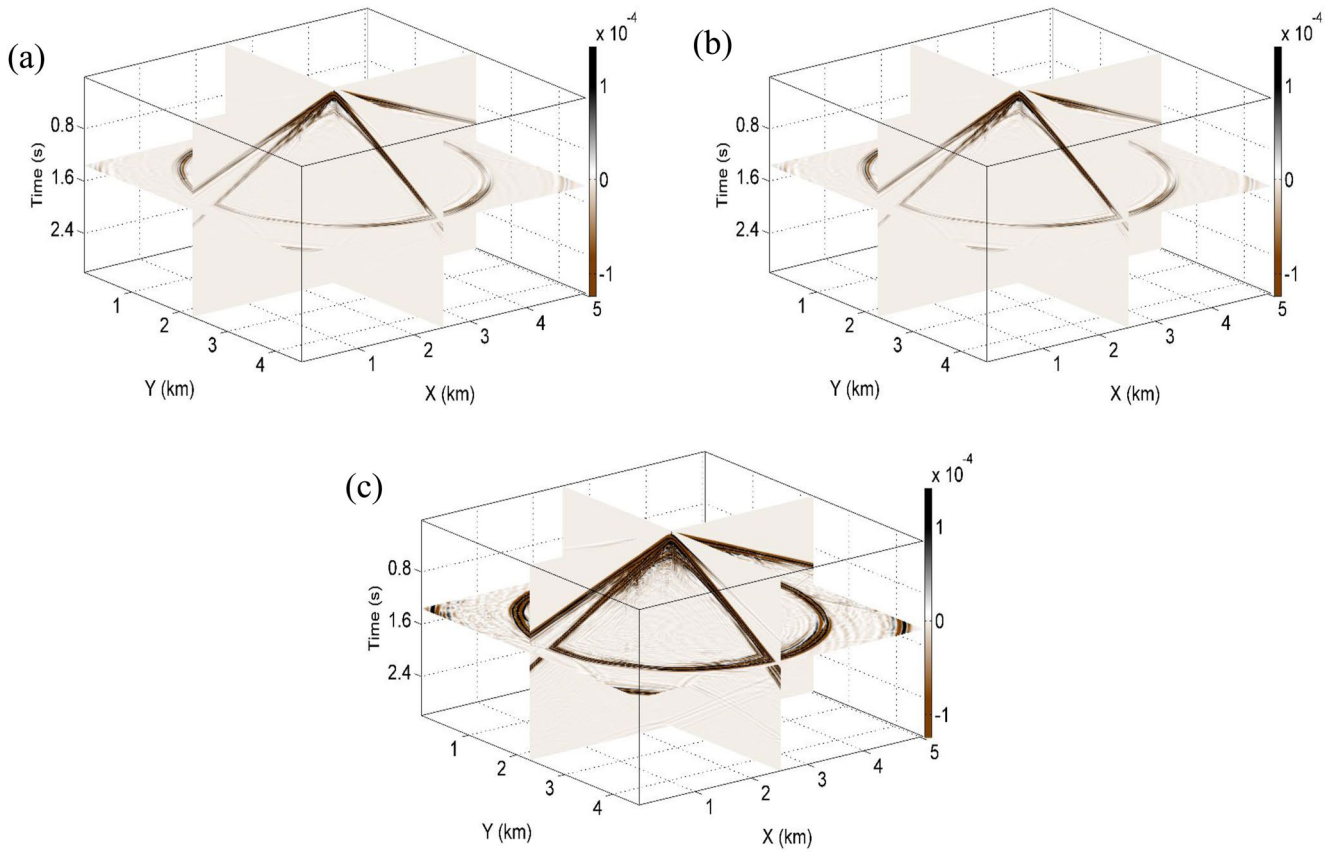

Figure 16. 3D common shot gathers generated by (a) our VTI-DFL viscoelastic wave equation, (b) the existing VTI-TF viscoelastic wave equation (Zhu, 2017), and (c) the VTI elastic wave equation.

$$\begin{cases} \rho \dfrac{\partial \mathbf{v}}{\partial t} - \mathbf{E}^{\mathrm{T}} \sigma = \mathbf{0}, \\ \dfrac{\partial \sigma}{\partial t} - \mathbf{L}\mathbf{E}\mathbf{v} = \mathbf{f}, \end{cases} \tag{A1}$$

where ρ is the density, $\mathbf{f}$ is the source function, $\mathbf{v} = \begin{bmatrix} v_x & v_y & v_z \end{bmatrix}^{\mathrm{T}}$ is the particle velocity, $\sigma = \begin{bmatrix} \sigma_{xx} & \sigma_{yy} & \sigma_{zz} & \sigma_{yz} & \sigma_{xz} & \sigma_{xy} \end{bmatrix}^{\mathrm{T}}$ represents the stress, and

$$\mathbf{E} = \begin{bmatrix} \frac{\partial}{\partial x} & 0 & 0 & 0 & \frac{\partial}{\partial z} & \frac{\partial}{\partial y} \\ 0 & \frac{\partial}{\partial y} & 0 & \frac{\partial}{\partial z} & 0 & \frac{\partial}{\partial x} \\ 0 & 0 & \frac{\partial}{\partial z} & \frac{\partial}{\partial y} & \frac{\partial}{\partial x} & 0 \end{bmatrix}^{\mathrm{T}}, \tag{A2}$$

for isotropic DFL viscoelastic wave equation, the attenuation coefficient matrix is

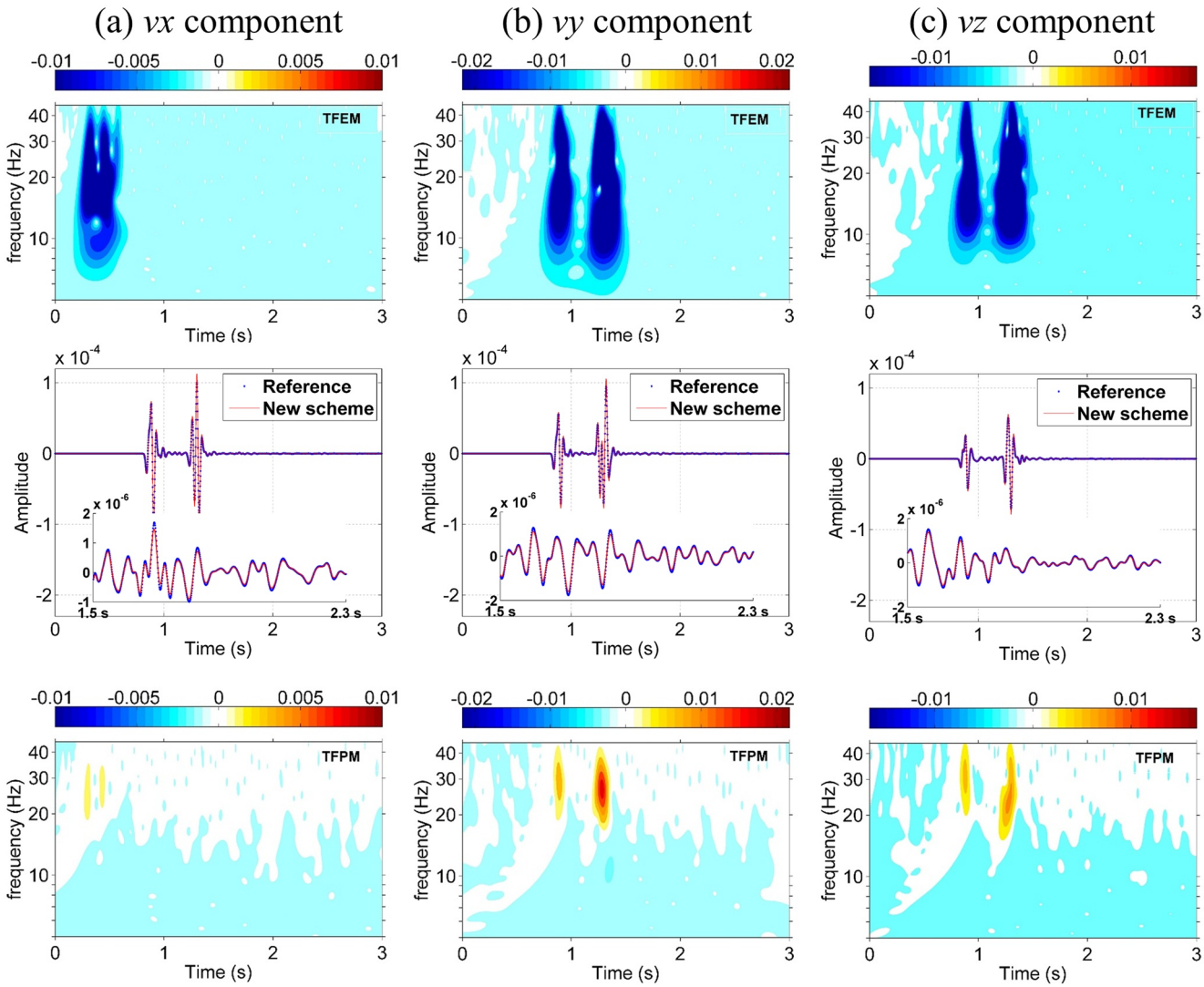

Figure 17. Waveforms comparison between the proposed VTI-DFL and the existing VTI-TF viscoelastic wave equations (middle row), time-frequency envelope (TFEM, top row), and the time-frequency phase misfit (TFPM, bottom row) of (a) v_x component, (b) v_y component, and (c) v_z component.

Table 3
Calculation-Time Comparison Between Different Simulation Schemes

Modeling examples	2D BP model	3D Salton model	3D Salton model
Size	500 × 270	252 × 227 × 24	505 × 455 × 48
Time steps	2,500	3,000	3,000
Fractional time (Matlab code)	4 hr 46 min	7 days 6 hr	_____
Fractional Laplacian (Matlab code)	11 min 21 s	2 hr 35 min	_____
Fractional Laplacian (CUDA code)	1 min 24 s	21 min	3 hr 18 min

$$\mathbf{L}=\begin{bmatrix} L_p & L_p\text{-}2L_s & L_p\text{-}2L_s & 0 & 0 & 0 \\ L_p\text{-}2L_s & L_p & L_p\text{-}2L_s & 0 & 0 & 0 \\ L_p\text{-}2L_s & L_p\text{-}2L_s & L_p & 0 & 0 & 0 \\ 0 & 0 & 0 & L_s & 0 & 0 \\ 0 & 0 & 0 & 0 & L_s & 0 \\ 0 & 0 & 0 & 0 & 0 & L_s \end{bmatrix}. \tag{A3}$$

The 3D VTI-DFL viscoelastic wave equation can be obtained by replacing the attenuation coefficient matrix, which is defined by

$$\mathbf{M}=\begin{bmatrix} M_{11} & M_{11}\text{-}2M_{66} & M_{13}+M_{11}-\bar{M}_{11} & 0 & 0 & 0 \\ M_{11}\text{-}2M_{66} & M_{11} & M_{13}+M_{11}-\bar{M}_{11} & 0 & 0 & 0 \\ M_{13}+M_{33}-\bar{M}_{33} & M_{13}+M_{33}-\bar{M}_{33} & M_{33} & 0 & 0 & 0 \\ 0 & 0 & 0 & M_{55} & 0 & 0 \\ 0 & 0 & 0 & 0 & M_{55} & 0 \\ 0 & 0 & 0 & 0 & 0 & M_{66} \end{bmatrix}. \tag{A4}$$

Note that the attenuation coefficients in Equations A3 and A4 have been defined in Equation 8 and Equation 37, respectively.

Appendix B: Decoupled Form of DFL and VTI-DFL Viscoelastic Wave Equations

The attenuation operator of the proposed DFL viscoelastic wave equation is shown in Equation 8. The benefit of the new derived DFL wave equation is the separation of amplitude loss and phase dispersion in the math expression. Following Chichinina et al. (2004) and Zhu and Carcione (2014), we can construct two separate wave equations to describe amplitude loss and phase dispersion, which is not possible with any conventional wave equation. For example, if the first and the third operators representing phase dispersion are eliminated, we can obtain a loss-dominated wave equation with the complex modulus of

$$L_{\theta,loss}=C_\theta\frac{1}{c_\theta^2}\left(d_{\theta,2}+d_{\theta,4}\left(-\nabla^2\right)^{-\frac{1}{2}}\frac{\partial}{\partial t}+d_{\theta,5}\frac{\partial}{\partial t}\right). \tag{B1}$$

The first three terms in Equation 8 form a dispersion-dominated wave equation. Its corresponding complex modulus is

$$L_{\theta,dis}=C_\theta\frac{1}{c_\theta^2}\left(d_{\theta,1}\left(-\nabla^2\right)^{-\frac{1}{2}}+d_{\theta,2}+d_{\theta,3}\left(-\nabla^2\right)^{\frac{1}{2}}\right). \tag{B2}$$

Equation 37 displays the attenuation operators of the VTI-DFL viscoelastic wave equation. With the same operations, we have the complex modulus of the loss-dominated wave equation

$$\begin{cases} M_{11,loss} = C_{11}\left(1+\dfrac{\pi\gamma_{11}}{c_{p\parallel}}\left(-\nabla^2\right)^{-\frac{1}{2}}\dfrac{\partial}{\partial t}+\dfrac{\pi\gamma_{11}^2}{\omega_0}\dfrac{\partial}{\partial t}\right) \\ M_{33,loss} = C_{33}\left(1+\dfrac{\pi\gamma_{33}}{c_{p\perp}}\left(-\nabla^2\right)^{-\frac{1}{2}}\dfrac{\partial}{\partial t}+\dfrac{\pi\gamma_{33}^2}{\omega_0}\dfrac{\partial}{\partial t}\right) \\ M_{55,loss} = C_{55}\left(1+\dfrac{\pi\gamma_{55}}{c_s}\left(-\nabla^2\right)^{-\frac{1}{2}}\dfrac{\partial}{\partial t}+\dfrac{\pi\gamma_{55}^2}{\omega_0}\dfrac{\partial}{\partial t}\right) \\ M_{13,loss} = C_{13}\left(1+\dfrac{\pi\gamma_{13}}{c_s}\left(-\nabla^2\right)^{-\frac{1}{2}}\dfrac{\partial}{\partial t}+\dfrac{\pi\gamma_{13}^2}{\omega_0}\dfrac{\partial}{\partial t}\right) \\ \bar{M}_{11,loss} = C_{11}\left(1+\dfrac{\pi\gamma_{11}}{c_s}\left(-\nabla^2\right)^{-\frac{1}{2}}\dfrac{\partial}{\partial t}+\dfrac{\pi\gamma_{11}^2}{\omega_0}\dfrac{\partial}{\partial t}\right) \\ \bar{M}_{33,loss} = C_{33}\left(1+\dfrac{\pi\gamma_{33}}{c_s}\left(-\nabla^2\right)^{-\frac{1}{2}}\dfrac{\partial}{\partial t}+\dfrac{\pi\gamma_{33}^2}{\omega_0}\dfrac{\partial}{\partial t}\right) \end{cases}, \tag{B3}$$

and the complex modulus of the dispersion-dominated wave equation

$$\begin{cases} M_{11,dis} = C_{11}\left(-\dfrac{\gamma_{11}\omega_0}{c_{p\parallel}}\left(-\nabla^2\right)^{-\frac{1}{2}}+1+\gamma_{11}\dfrac{c_{p\parallel}}{\omega_0}\left(-\nabla^2\right)^{\frac{1}{2}}\right) \\ M_{33,dis} = C_{33}\left(-\dfrac{\gamma_{33}\omega_0}{c_{p\perp}}\left(-\nabla^2\right)^{-\frac{1}{2}}+1+\gamma_{33}\dfrac{c_{p\perp}}{\omega_0}\left(-\nabla^2\right)^{\frac{1}{2}}\right) \\ M_{55,dis} = C_{55}\left(-\dfrac{\gamma_{55}\omega_0}{c_s}\left(-\nabla^2\right)^{-\frac{1}{2}}+1+\gamma_{55}\dfrac{c_s}{\omega_0}\left(-\nabla^2\right)^{\frac{1}{2}}\right) \\ M_{13,dis} = C_{13}\left(-\dfrac{\gamma_{13}\omega_0}{c_s}\left(-\nabla^2\right)^{-\frac{1}{2}}+1+\gamma_{13}\dfrac{c_s}{\omega_0}\left(-\nabla^2\right)^{\frac{1}{2}}\right) \\ \bar{M}_{11,dis} = C_{11}\left(-\dfrac{\gamma_{11}\omega_0}{c_s}\left(-\nabla^2\right)^{-\frac{1}{2}}+1+\gamma_{11}\dfrac{c_s}{\omega_0}\left(-\nabla^2\right)^{\frac{1}{2}}\right) \\ \bar{M}_{33,dis} = C_{33}\left(-\dfrac{\gamma_{33}\omega_0}{c_s}\left(-\nabla^2\right)^{-\frac{1}{2}}+1+\gamma_{33}\dfrac{c_s}{\omega_0}\left(-\nabla^2\right)^{\frac{1}{2}}\right) \end{cases}. \tag{B4}$$

Appendix C: Analytical Solutions Obtained by Solving Viscoelastic Christoffel Equation

The viscoelastic Christoffel equation in TI media are solved in the frequency-wavenumber domain

$$\left(K^2\mathbf{G}-\rho\omega^2\mathbf{I}\right)\mathbf{U}=0, \tag{C1}$$

where $K = k - \alpha i$ represents the complex wavenumber, α is the attenuation coefficient, $\mathbf{G}$ is the complex-valued Christoffel matrix, $\mathbf{I}$ is the identity matrix and $\mathbf{U}$ denotes the general viscoelastic plane wave solutions. Setting characteristic determinant of formula C1 equal to zero, we obtain the following complex velocities (Carcione, 2014)

$$
\begin{aligned}
v_{SH}(\theta) &= \sqrt{\rho^{-1}\left(\tilde{C}_{66}\sin^2\theta + \tilde{C}_{55}\cos^2\theta\right)} \\
v_{qS}(\theta) &= \sqrt{(2\rho)^{-1}\left(\tilde{C}_{11}\sin^2\theta + \tilde{C}_{33}\cos^2\theta + \tilde{C}_{55} - A\right)} \\
v_{qP}(\theta) &= \sqrt{(2\rho)^{-1}\left(\tilde{C}_{11}\sin^2\theta + \tilde{C}_{33}\cos^2\theta + \tilde{C}_{55} + A\right)},
\end{aligned} \tag{C2}
$$

with

$$
A = \sqrt{\left[\left(\tilde{C}_{11} - \tilde{C}_{55}\right)\sin^2\theta + \left(\tilde{C}_{55} - \tilde{C}_{33}\right)\cos^2\theta\right]^2 + 4\left(\tilde{C}_{13} + \tilde{C}_{55}\right)^2\sin^2\theta\cos^2\theta}, \tag{C3}
$$

where θ is the propagation angle between the wavenumber vector and the symmetry axis. The complex-value stiffness coefficients $\tilde{C}_{ij}$ have been defined in Equation 25. The analytical solutions of direction-dependent phase velocities and quality factors by Equation C2, it gives

$$
v_m^{ph}(\theta) = \left[\mathrm{Re}\left(\frac{1}{v_m(\theta)}\right)\right]^{-1}, \tag{C4}
$$

$$
Q_m(\theta) = \frac{\mathrm{Re}\left(v_m^2(\theta)\right)}{\mathrm{Im}\left(v_m^2(\theta)\right)}, m = qP, qS, SH. \tag{C5}
$$

Appendix D: Eigenvalues of Attenuation Operator Matrix in DFL/VTI-DFL Wave Equations

The attenuation operator matrix of the second-order VTI-DFL viscoelastic wave equation is

$$
\tilde{\mathbf{B}} = \frac{1}{\rho}\begin{bmatrix}
G_1k_x^2 + G_5k_z^2 & (G_2+G_5)k_xk_z & 0 & 0 & 0 \\
(G_4+G_5)k_xk_z & G_5k_X^2 + G_3k_z^2 & 0 & 0 & 0 \\
0 & 0 & G_1k_x^2 & G_2k_z^2 & (G_1+G_2)k_xk_z \\
0 & 0 & G_4k_x^2 & G_3k_z^2 & (G_3+G_4)k_xk_z \\
0 & 0 & G_5k_xk_z & G_5k_xk_z & G_5\left(k_x^2+k_z^2\right)
\end{bmatrix}, \tag{D1}
$$

with

$$
\begin{cases}
G_1 = C_{11}\left(-\dfrac{\gamma_{11}\omega_0}{c_{p11}k} + 1 + \dfrac{\gamma_{11}c_{p11}k}{\omega_0} + \left(\dfrac{\pi\gamma_{11}}{c_{p11}k} + \dfrac{\pi\gamma_{11}^2}{\omega_0}\right)ivk\right) \\
G_3 = C_{33}\left(-\dfrac{\gamma_{33}\omega_0}{c_{p\perp}k} + 1 + \dfrac{\gamma_{33}c_{p\perp}k}{\omega_0} + \left(\dfrac{\pi\gamma_{33}}{c_{p\perp}k} + \dfrac{\pi\gamma_{33}^2}{\omega_0}\right)ivk\right) \\
G_5 = C_{55}\left(-\dfrac{\gamma_{55}\omega_0}{c_sk} + 1 + \dfrac{\gamma_{55}c_sk}{\omega_0} + \left(\dfrac{\pi\gamma_{55}}{c_sk} + \dfrac{\pi\gamma_{55}^2}{\omega_0}\right)ivk\right) \\
G_{13} = C_{13}\left(-\dfrac{\gamma_{13}\omega_0}{c_sk} + 1 + \dfrac{\gamma_{13}c_sk}{\omega_0} + \left(\dfrac{\pi\gamma_{13}}{c_sk} + \dfrac{\pi\gamma_{13}^2}{\omega_0}\right)ivk\right) \\
\bar{G}_1 = C_{11}\left(-\dfrac{\gamma_{11}\omega_0}{c_sk} + 1 + \dfrac{\gamma_{11}c_sk}{\omega_0} + \left(\dfrac{\pi\gamma_{11}}{c_sk} + \dfrac{\pi\gamma_{11}^2}{\omega_0}\right)ivk\right) \\
\bar{G}_3 = C_{33}\left(-\dfrac{\gamma_{33}\omega_0}{c_sk} + 1 + \dfrac{\gamma_{33}c_sk}{\omega_0} + \left(\dfrac{\pi\gamma_{33}}{c_sk} + \dfrac{\pi\gamma_{33}^2}{\omega_0}\right)ivk\right) \\
G_2 = G_{13} - \bar{G}_1 + G_1 \\
G_4 = G_{13} - \bar{G}_3 + G_3
\end{cases}, \tag{D2}
$$

where $v = \max\{c_{p\parallel}, c_{p\perp}, c_s\}$. The eigenvalues of formula D1 is

$$\begin{cases} \lambda_1 = 0 \\ \lambda_{2,3,4,5} = \dfrac{1}{2\rho}\left\{ \pm \sqrt{\begin{array}{c} G_1 k_x^2 + G_3 k_z^2 + G_5\left(k_x^2 + k_z^2\right) \\ \left(G_1 k_x^2 + G_3 k_z^2 + G_5 k_x^2 + G_5 k_z^2\right) \\ -4G_5\left[\left(G_1 k_x^4 + G_3 k_z^4\right) - \left(G_2 + G_4\right) k_x^2 k_z^2\right] \\ + \left(G_2 G_4 - G_1 G_3\right) k_x^2 k_z^2 \end{array}} \right\} \end{cases}. \tag{D3}$$

The attenuation operator matrix of the second-order DFL viscoelastic wave equation is

$$\tilde{\mathbf{B}} = \frac{1}{\rho}\begin{bmatrix} D_p k_x^2 + D_s k_z^2 & \left(D_p - D_s\right) k_x k_z & 0 & 0 & 0 \\ \left(D_p - D_s\right) k_x k_z & D_p k_z^2 + D_s k_x^2 & 0 & 0 & 0 \\ 0 & 0 & D_p k_x^2 & \left(D_p - 2D_s\right) k_z^2 & 2\left(D_p - D_s\right) k_x k_z \\ 0 & 0 & \left(D_p - 2D_s\right) k_x^2 & D_p k_z^2 & 2\left(D_p - D_s\right) k_x k_z \\ 0 & 0 & D_s k_x k_z & D_s k_x k_z & D_s\left(k_x^2 + k_z^2\right) \end{bmatrix}, \tag{D4}$$

with

$$D_\theta = C_\theta \frac{1}{c_\theta^2}\left(d_{\theta,1} k^{-1} + d_{\theta,2} + d_{\theta,3} k + \left(d_{\theta,4} k^{-1} + d_{\theta,5}\right) ivk\right), (\theta = p \text{ or } s) \tag{D5}$$

where $v = \max\{c_p, c_s\}$. The eigenvalues of formula D4 is

$$\begin{cases} \lambda_1 = 0 \\ \lambda_{2,3} = \dfrac{1}{\rho} D_p k^2 \\ \lambda_{4,5} = \dfrac{1}{\rho} D_s k^2 \end{cases}. \tag{D6}$$

Data Availability Statement

The original Salton Trough velocity model can be freely accessed on https://www.geol.lsu.edu/persaud/Data.html. The 3D simulation code with examples can be found at https://zenodo.org/record/5548874.

Acknowledgments
We appreciate the Editor, Michael Bostock, and the Associate Editor, for handling this manuscript. We would like to thank the reviewers, Peter Moczo and another anonymous reviewer, for their valuable suggestions that have significantly improved the manuscript. This work is partly supported by the National Natural Science Foundation of China (41930431, 41630314, U19B6003-04), Local Universities Reformation and Development Personnel Training Supporting Project from Central Authorities (140119001), National Key R & D Program of China (2018YFA0702502), and the Joint Guiding Project of the Natural Science Foundation of Heilongjiang Province (LH2021D009).

References

Ajala, R., Persaud, P., Stock, J. M., Fuis, G. S., Hole, J. A., Goldman, M., & Scheirer, D. (2019). Three-dimensional basin and fault structure from a detailed seismic velocity model of Coachella Valley, Southern California. *Journal of Geophysical Research: Solid Earth*, *124*(5), 4728–4750. https://doi.org/10.1029/2018jb016260

Aki, K. (1980). Attenuation of shear-waves in the lithosphere for frequencies from 0.05 to 25 Hz. *Physics of the Earth and Planetary Interiors*, *21*(1), 50–60. https://doi.org/10.1016/0031-9201(80)90019-9

Alkhalifah, T. (2000). An acoustic wave equation for anisotropic media. *Geophysics*, *65*(4), 1239–1250. https://doi.org/10.1190/1.1444815

Anderson, D. L. (1989). *Theory of the earth*. Blackwell scientific publications.

Bai, T., & Tsvankin, I. (2016). Time-domain finite-difference modeling for attenuative anisotropic media. *Geophysics*, *81*(2), C69–C77. https://doi.org/10.1190/geo2015-0424.1

Bao, X., Song, X., Eaton, D. W., Xu, Y., & Chen, H. (2020). Episodic lithospheric deformation in eastern Tibet inferred from seismic anisotropy. *Geophysical Research Letters*, *47*(3). https://doi.org/10.1029/2019gl085721

Blanch, J. O., Robertsson, J. O. A., & Symes, W. W. (1995). Modeling of a constant Q: Methodology and algorithm for an efficient and optimally inexpensive viscoelastic technique. *Geophysics*, *60*(1), 176–184. https://doi.org/10.1190/1.1443744

Caputo, M. (1967). Linear models of dissipation whose Q is almost frequency independent-II. *Geophysical Journal International*, *13*(5), 529–539. https://doi.org/10.1111/j.1365-246x.1967.tb02303.x

Caputo, M., Carcione, J. M., & Cavallini, F. (2011). Wave simulation in biologic media based on the Kelvin-Voigt fractional-derivative stress-strain relation. *Ultrasound in Medicine and Biology*, *37*(6), 996–1004. https://doi.org/10.1016/j.ultrasmedbio.2011.03.009

Carcione, J. (2007). *Handbook of Geophysical exploration*. Wave fields in real media: Wave propagation in anisotropic, anelastic, porous and electromagnetic media. Elsevier Science.

Carcione, J. M. (1990). Wave propagation in anisotropic linear viscoelastic media: Theory and simulated wavefield. *Geophysical Journal International*, *101*(3), 739–750. https://doi.org/10.1111/j.1365-246x.1990.tb05580.x

Carcione, J. M. (1992). Anisotropic Q and velocity dispersion of finely layered media1. *Geophysical Prospecting*, *40*(7), 761–783. https://doi.org/10.1111/j.1365-2478.1992.tb00551.x

Carcione, J. M. (1995). Constitutive model and wave equations for linear, viscoelastic, anisotropic media. *Geophysics*, *60*(2), 537–548. https://doi.org/10.1190/1.1443791

Carcione, J. M. (2014). *Wave fields in real media: Theory and numerical simulation of wave propagation in anisotropic, anelastic, porous and electromagnetic media* (3rd ed.). Elsevier.

Carcione, J. M., Kosloff, D., & Kosloff, R. (1988). Wave propagation simulation in a linear viscoacoustic medium. *Geophysical Journal of the Royal Astronomical Society*, *93*(2), 393–401. https://doi.org/10.1111/j.1365-246x.1988.tb02010.x

Chen, H., Zhou, H., & Rao, Y. (2020). Source wavefield reconstruction in fractional Laplacian viscoacoustic wave equation-based full waveform inversion. *IEEE Transactions on Geoscience and Remote Sensing*.

Chen, H. M., Zhou, H., Li, Q. Q., & Wang, Y. F. (2016). Two efficient modeling schemes for fractional Laplacian viscoacoustic wave equation. *Geophysics*, *81*(5), T233–T249. https://doi.org/10.1190/geo2015-0660.1

Chen, W., & Holm, S. (2004). Fractional Laplacian time-space models for linear and nonlinear lossy media exhibiting arbitrary frequency power-law dependency. *Journal of the Acoustical Society of America*, *115*(4), 1424–1430. https://doi.org/10.1121/1.1646399

Chichinina, T., Obolentseva, I., Gik, L., Bobrov, B., & Ronquillo-Jarillo, G. (2009). Attenuation anisotropy in the linear-slip model: Interpretation of physical modeling data. *Geophysics*, *74*(5), WB165–WB176. https://doi.org/10.1190/1.3173806

Chichinina, T., Sabinin, V., & Ronquillo-Jarillo, G. (2004). *P-wave attenuation anisotropy in fracture characterization: Numerical modeling for reflection data: 74th Annual International Meeting* (pp. 143–146). SEG.

Day, S. M., & Minster, J. B. (1984). Numerical simulation of attenuated wavefields using a Padé approximant method. *Geophysical Journal International*, *78*(1), 105–118. https://doi.org/10.1111/j.1365-246x.1984.tb06474.x

Emmerich, H., & Korn, M. (1987). Incorporation of attenuation into time-domain computations of seismic wave fields. *Geophysics*, *52*(9), 1252–1264. https://doi.org/10.1190/1.1442386

Fichtner, A., & Van Driel, M. (2014). Models and Fréchet kernels for frequency-(in) dependent Q. *Geophysical Journal International*, *198*(3), 1878–1889. https://doi.org/10.1093/gji/ggu228

Gazdag, J. (1981). Modeling of the acoustic wave equation with transform methods. *Geophysics*, *46*(6), 854–859. https://doi.org/10.1190/1.1441223

Guo, P., & McMechan, G. A. (2017). Sensitivity of 3D 3C synthetic seismograms to anisotropic attenuation and velocity in reservoir models. *Geophysics*, *82*(2), T79–T95. https://doi.org/10.1190/geo2016-0321.1

Hosten, B., Deschamps, M., & Tittmann, B. (1987). Inhomogeneous wave generation and propagation in lossy anisotropic solids: Application to the characterization of viscoelastic composite materials. *Journal of the Acoustical Society of America*, *82*(5), 1763–1770. https://doi.org/10.1121/1.395170

Kjartansson, E. (1979). Constant Q-wave propagation and attenuation. *Journal of Geophysical Research*, *84*(B9), 4737–4748. https://doi.org/10.1029/jb084ib09p04737

Komatitsch, D., Barnes, C., & Tromp, J. (2000). Simulation of anisotropic wave propagation based upon a spectral element method. *Geophysics*, *65*(4), 1251–1260. https://doi.org/10.1190/1.1444816

Komatitsch, D., & Martin, R. (2007). An unsplit convolutional perfectly matched layer improved at grazing incidence for the seismic wave equation. *Geophysics*, *72*(5), SM155–SM167. https://doi.org/10.1190/1.2757586

Kristek, J., & Moczo, P. (2003). Seismic-wave propagation in viscoelastic media with material discontinuities: A 3D fourth-order staggered-grid finite-difference modeling. *Bulletin of the Seismological Society of America*, *93*(5), 2273–2280. https://doi.org/10.1785/0120030023

Kristek, J., Moczo, P., Chaljub, E., & Kristekova, M. (2019). A discrete representation of a heterogeneous viscoelastic medium for the finite-difference modelling of seismic wave propagation. *Geophysical Journal International*, *217*(3), 2021–2034. https://doi.org/10.1093/gji/ggz132

Kristekova, M., Kristek, J., & Moczo, P. (2009). Time-frequency misfit and goodness-of-fit criteria for quantitative comparison of time signals. *Geophysical Journal International*, *178*(2), 813–825. https://doi.org/10.1111/j.1365-246x.2009.04177.x

Kristekova, M., Kristek, J., Moczo, P., & Day, S. M. (2006). Misfit criteria for quantitative comparison of seismograms. *Bulletin of the Seismological Society of America*, *96*(5), 1836–1850. https://doi.org/10.1785/0120060012

Lee, J. Y., & Greengard, L. (2005). The type 3 nonuniform FFT and its applications. *Journal of Computational Physics*, *206*(1), 1–5. https://doi.org/10.1016/j.jcp.2004.12.004

Li, J. X., Zheng, Y. C., Thomsen, L. J., Fang, X. D., & Fang, X. (2018). Deep earthquakes in subducting slabs hosted in highly anisotropic rock fabric. *Nature Geoscience*, *11*, 696–700. https://doi.org/10.1038/s41561-018-0188-3

Li, Q., Fu, L. Y., Zhou, H., Wei, W., & Hou, W. (2019). Effective Q-compensated reverse time migration using new decoupled fractional Laplacian viscoacoustic wave equation. *Geophysics*, *84*(2), S57–S69. https://doi.org/10.1190/geo2017-0748.1

Li, Q. Q., Zhou, H., Zhang, Q. C., Chen, H. M., & Sheng, S. B. (2016). Efficient reverse time migration based on fractional Laplacian viscoacoustic wave equation. *Geophysical Journal International*, *204*(1), 488–504. https://doi.org/10.1093/gji/ggv456

Li, Q. Z. (1993). *High resolution seismic data Processing*. Petroleum Industry Press.

Liu, E., Crampin, S., Queen, J. H., & Rizer, W. D. (1993). Velocity and attenuation anisotropy caused by microcracks and microfractures in a multiazimuth reverse VSP. *Canadian Journal of Exploration Geophysics*, *29*(1), 177–188.

Liu, H. P., Anderson, D. L., & Kanamori, H. (1976). Velocity dispersion due to anelasticity; implications for seismology and mantle composition. *Geophysical Journal International*, *47*(1), 41–58. https://doi.org/10.1111/j.1365-246x.1976.tb01261.x

Lynn, H. B., Campagna, D., Simon, K. M., & Beckham, W. E. (1999). Relationship of P-wave seismic attributes, azimuthal anisotropy, and commercial gas pay in 3-d P-wave multiazimuth data, Rulison field, Piceance basin, Colorado. *Geophysics*, *64*(4), 1293–1311. https://doi.org/10.1190/1.1444635

Mainardi, F. (2010). *Fractional calculus and waves in linear viscoelasticity: An Introduction to Mathematical Models*. World Scientific.

Mäkinen, A. M., Deuss, A., & Redfern, S. A. (2014). Anisotropy of Earth's inner core intrinsic attenuation from seismic normal mode models. *Earth and Planetary Science Letters*, *404*, 354–364.

McDonal, F., Angona, F., Mills, R., Sengbush, R., Van Nostrand, R., & White, J. (1958). Attenuation of shear and compressional waves in Pierre shale. *Geophysics*, *23*(3), 421–439. https://doi.org/10.1190/1.1438489

Moczo, P., & Kristek, J. (2005). On the rheological models used for time-domain methods of seismic wave propagation. *Geophysical Research Letters*, *32*(1). https://doi.org/10.1029/2004gl021598

Moczo, P., Kristek, J., & Gális, M. (2014). *The finite-difference modelling of earthquake motions: Waves and ruptures*. Cambridge University Press.

Moczo, P., Kristek, J., Vavrycuk, V., Archuleta, R. J., & Halada, L. (2002). 3D heterogeneous staggered-grid finite-difference modeling of seismic motion with volume harmonic and arithmetic averaging of elastic moduli and densities. *Bulletin of the Seismological Society of America*, *92*(8), 3042–3066. https://doi.org/10.1785/0120010167

Mu, X., Huang, J., Yang, J., Li, Z., & Ivan, M. S. (2021). *Viscoelastic wave propagation simulation using new spatial variable-order fractional Laplacians*. Bulletin of the Seismological Society of America.

Nabighian, M. N. (Ed.). (1988). *Electromagnetic methods in applied Geophysics: Volume 1, theory*. Society of Exploration Geophysicists.

Piane, C. D., Sarout, J., Madonna, C., Saenger, E. H., Dewhurst, D., & Raven, M. (2014). Frequency-dependent seismic attenuation in shales: Experimental results and theoretical analysis. *Geophysical Journal International*, *198*, 504–515. https://doi.org/10.1093/gji/ggu148

Qiao, Z., Sun, C., & Wu, D. (2019). Theory and modelling of constant-Q viscoelastic anisotropic media using fractional derivative. *Geophysical Journal International*, *217*(2), 798–815. https://doi.org/10.1093/gji/ggz050

Robertsson, J. O. A., Blanch, J. O., & Symes, W. W. (1994). Viscoelastic finite-difference modeling. *Geophysics*, *59*(9), 1444–1456. https://doi.org/10.1190/1.1443701

Romanowicz, B., & Wenk, H. (2017). Anisotropy in the deep Earth. *Physics of the Earth and Planetary Interiors*, *269*, 58–90. https://doi.org/10.1016/j.pepi.2017.05.005

Savage, B., Komatitsch, D., & Tromp, J. (2010). Effects of 3D attenuation on seismic wave amplitude and phase measurements. *Bulletin of the Seismological Society of America*, *100*(3), 1241–1251. https://doi.org/10.1785/0120090263

Spencer, J. W., Jr. (1981). Stress relaxations at low frequencies in fluid-saturated rocks: Attenuation and modulus dispersion. *Journal of Geophysical Research*, *86*(B3), 1803–1812. https://doi.org/10.1029/jb086ib03p01803

Stein, S., & Wysession, M. (2003). *An introduction to seismology, earthquakes and earth structure*. Blackwell Publishing.

Sun, J. Z., Zhu, T. Y., & Fomel, S. (2015). Viscoacoustic modeling and imaging using low-rank approximation. *Geophysics*, *80*(5), A103–A108. https://doi.org/10.1190/geo2015-0083.1

Tao, G., & King, M. S. (1990). Shear-wave velocity and Q anisotropy in rocks: A laboratory study. *International Journal of Rock Mechanics and Mining Sciences & Geomechanics Abstracts*, *27*(5), 353–361. https://doi.org/10.1016/0148-9062(90)92710-v

Thomsen, L. (1986). Weak elastic anisotropy. *Geophysics*, *51*(10), 1954–1966. https://doi.org/10.1190/1.1442051

Treeby, B. E., & Cox, B. (2010). Modeling power law absorption and dispersion for acoustic propagation using the fractional Laplacian. *Journal of the Acoustical Society of America*, *127*(5), 2741–2748. https://doi.org/10.1121/1.3377056

Tsvankin, I. (2012). *Seismic signatures and analysis of reflection data in anisotropic media* (3rd ed.). Society of Exploration Geophysicists.

Wang, N., Zhou, H., Chen, H. M., Xia, M. M., Wang, S. C., Fang, J. W., & Sun, P. Y. (2018). A constant fractional-order viscoelastic wave equation and its numerical simulation scheme. *Geophysics*, *83*(1), T39–T48. https://doi.org/10.1190/geo2016-0609.1

Wang, N., Zhu, T., Zhou, H., Chen, H., Zhao, X., & Tian, Y. (2020). Fractional Laplacians viscoacoustic wavefield modeling with k-space-based time-stepping error compensating scheme. *Geophysics*, *85*(1), T1–T13. https://doi.org/10.1190/geo2019-0151.1

Wang, W., McMechan, G. A., Tang, C., & Xie, F. (2016). Up/down and P/S decompositions of elastic wavefields using complex seismic traces with applications to calculating Poynting vectors and angle-domain common-image gathers from reverse time migrations Elastic up/down and P/S decompositions. *Geophysics*, *81*(4), S181–S194. https://doi.org/10.1190/geo2015-0456.1

Wang, Y. F., Zhou, H., Chen, H. M., & Chen, Y. K. (2017). Adaptive stabilization for Q-compensated reverse time migration. *Geophysics*, *83*(1), S15–S32.

Xing, G., & Zhu, T. (2019). Modeling frequency-independent Q viscoacoustic wave propagation in heterogeneous media. *Journal of Geophysical Research: Solid Earth*, *124*(11), 11568–11584. https://doi.org/10.1029/2019jb017985

Xing, G., & Zhu, T. (2020). *Hessian-based multiparameter fractional viscoacoustic full-waveform inversion*. SEG Technical Program Expanded Abstracts.

Xing, G., & Zhu, T. (2022). Decoupled Fréchet kernels based on a fractional viscoacoustic wave equation. *Geophysics*, *87*(1), T61–T70. https://doi.org/10.1190/geo2021-0248.1

Xue, Z., Sun, J., Fomel, S., & Zhu, T. (2017). Accelerating full-waveform inversion with attenuation compensation. *Geophysics*, *83*(1), A13–A20.

Yang, J., & Zhu, H. (2018). A time-domain complex-valued wave equation for modelling viscoacoustic wave propagation. *Geophysical Journal International*, *215*(2), 1064–1079. https://doi.org/10.1093/gji/ggy323

Yang, J., Zhu, H., Li, X., Ren, L., & Zhang, S. (2020). Estimating p wave velocity and attenuation structures using full waveform inversion based on a time domain complex-valued viscoacoustic wave equation: The method. *Journal of Geophysical Research: Solid Earth*, *125*. https://doi.org/10.1029/2019jb019129

Yao, J., Zhu, T., Hussain, F., & Kouri, D. J. (2016). Locally solving fractional laplacian viscoacoustic wave equation using hermite distributed approximating functional method. *Geophysics*, *82*(2), T59–T67.

Yu, W., & Wen, L. (2006). Inner core attenuation anisotropy. *Earth and Planetary Science Letters*, *245*, 581–594. https://doi.org/10.1016/j.epsl.2006.03.043

Zahradník, J., Moczo, P., & Hron, F. (1993). Testing four elastic finite difference schemes for behaviour at discontinuities. *Bulletin of the Seismological Society of America*, *83*, 107–129.

Zhang, Y., Liu, Y., & Xu, S. (2020). Viscoelastic wave simulation with high Temporal accuracy using frequency-dependent complex velocity. *Surveys in Geophysics*, 1–36. https://doi.org/10.1007/s10712-020-09607-3

Zhao, X. B., Zhou, H., Wang, Y. F., Chen, H. M., Zhou, Z., Sun, P. Y., & Zhang, J. L. (2018). A stable approach for Q-compensated viscoelastic reverse time migration using excitation amplitude imaging condition. *Geophysics*, *83*(5), S459–S476. https://doi.org/10.1190/geo2018-0222.1

Zhu, T. Y. (2017). Numerical simulation of seismic wave propagation in viscoelastic-anisotropic media using frequency-independent Q wave equation. *Geophysics*, *82*(4). WA1–WA10. https://doi.org/10.1190/geo2016-0635.1

Zhu, T. Y., & Bai, T. (2019). Efficient modeling of wave propagation in a vertical transversely isotropic attenuative medium based on fractional Laplacian. *Geophysics*, *84*(3), T121–T131. https://doi.org/10.1190/geo2018-0538.1

Zhu, T. Y., & Carcione, J. M. (2014). Theory and modelling of constant-Q P-and S-waves using fractional spatial derivatives. *Geophysical Journal International*, *196*(3), 1787–1795. https://doi.org/10.1093/gji/ggt483

Zhu, T. Y., Carcione, J. M., & Harris, J. M. (2013). Approximating constant-Q seismic propagation in the time domain. *Geophysical Prospecting*, *61*(5), 931–940. https://doi.org/10.1111/1365-2478.12044

Zhu, T. Y., & Harris, J. M. (2014). Modeling acoustic wave propagation in heterogeneous attenuating media using decoupled fractional Laplacians. *Geophysics*, *79*(3), T105–T116. https://doi.org/10.1190/geo2013-0245.1

Zhu, T. Y., Harris, J. M., & Biondi, B. (2014). Q-compensated reverse time migration. *Geophysics*, *79*(3), S77–S87. https://doi.org/10.1190/geo2013-0344.1

Zhu, T. Y., & Sun, J. Z. (2017). Viscoelastic reverse-time migration with attenuation compensation. *Geophysics*, *82*(2), S61–S73. https://doi.org/10.1190/geo2016-0239.1

Zhu, Y., & Tsvankin, I. (2006). Plane-wave propagation in attenuative transversely isotropic media. *Geophysics*, *71*(2), T17–T30. https://doi.org/10.1190/1.2187792

Zhubayev, A., Houben, M. E., Smeulders, D. M. J., & Barnhoorn, A. (2016). Ultrasonic velocity and attenuation anisotropy of shales, Whitby, United Kingdom. *Geophysics*, *81*(1), D45–D56. https://doi.org/10.1190/geo2015-0211.1